Stony Brook University

Numerical Modeling and Combustion Studies of Scramjet Problem

A Dissertation presented

by

Ying Xu

to

The Graduate School

in Partial Fulfillment of the

Requirements

for the Degree of

Doctor of Philosophy

in

Applied Mathematics and Statistic

Stony Brook University

December 2014

Stony Brook University
The Graduate School
Ying Xu
We, the dissertation committee for the above candidate for the
Doctor of Philosophy degree, hereby recommend
acceptance of this dissertation

James Glimm - Dissertation Advisor
Professor of Applied Mathematics and Statistics

Xiangmin Jiao - Chairperson of Defense
Associate Professor of Applied Mathematics and Statistics

Roman Samulyak
Professor of Applied Mathematics and Statistics

Michael McGuigan
Deputy Director, Computational Scientist

This dissertation is accepted by the Graduate School

Charles Taber
Dean of the Graduate School

Numerical Modeling and Combustion Studies of Scramjet Problem

by

Ying Xu

Doctor of Philosophy

in

Applied Mathematics and Statistic

Stony Brook University

2014

Abstract

Physical and numerical modeling of turbulent mixing and turbulent combustion in a Scramjet combustion chamber is studied. A high-order finite volume scheme is applied to the flow, accompanied with dynamic subgrid-

scale model and local averaging procedure to account for the effect of unresolved small length scales turbulent fluid behavior. The Arrhenius law kinetic mechanism is applied to describe the nonlinearity of chemical reactions. To model combustion, the finite rate chemistry is developed to characterize the combustion process inside the combustion chamber. Results are compared among the finite rate model, the flamelet model/progress variable approach adopted by Stanford PSAAP center and experimental data. Since the mesh requirement to resolve the flame front is too strict for most combustion simulation applications, the thickened flame model that artificially expands the flame front is investigated. The effectiveness of the model is studied in a one-dimensional context and applied to the three-dimensional Scramjet simulation. The feasible level of thickening factor is determined to assume that the major flame features should be preserved. The model is further extended to dynamic thickened flame to account for the coexistence of premixed and diffusion flame in the combustion chamber. It is extended to a reduced chemical mechanism to reduce the time complexity needed to solve chemistry.

Table of Contents

Contents

List of Figures

List of Tables

Acknowledgements

I would like to express my deepest gratitude and thanks to my advisor Professor James Glimm, for the guidance, support and encouragement he gave me throughout all these years of my study and research. It has been a great honor for me to work with him, and I have learned not only the correct way to carry out research, but also the spirit to become a professional. I would never have been able to finish this work without all the help and suggestions he gave me. I have also been deeply encouraged by the enthusiasm he has towards scientific research. That leads me to believe that one of the most important things in life is to find what one is passionate about, and keep at it.

I would also like to thank the other three committee members, Professor Xiangmin Jiao, Professor Roman Samulyak, and Dr. Michael McGuigan from Brookhaven National Laboratory, not only for their kindness and patience, but also for the great comments, suggestions and constructive feedback they gave me.

Also, I'm very thankful to the researchers at the Center for Turbulence Research, Stanford University, among them, Professor Johan Larsson, Professor Mirko Gamba and Professor Godfrey Mungal, for their generosity in sharing insightful ideas and research progress with us. It has been a great experience to learn so much from them.

I would like to express my special thanks to my teammate, Xiaoxue Gong,

for all these years of collaborative work and helpful comments. Also, to all my friends, colleagues, and office mates, including Dr. Hyunkyung Lim, Dr. Yan Yu, Yating Huang, Vinay Mahadeo, Shuai Xue, Wenlin Hu and Qiangqiang Shi, for the long-lasting friendship and the great time we have shared. The time and memory will stay with me forever.

Through all these years, the constant support and love from my parents have always been the greatest comfort for me. All I have accomplished are attributed to them. They are the most important people in my life, and this work is dedicated to them.

1 Introduction

1.1 Background and Overview

Scramjet (Supersonic Combustion Ramjet) is a type of engine that operates under supersonic airflow conditions. The efficiency in its propulsion system over ramjet has made it a very active research topic over the past decades. The flow structure inside a scramjet combustion chamber is an extension of the jet in crossflow (JICF) configuration, which categorizes a type of flow regime that is frequently encountered in many practical applications. For many years, a large body of literature has been devoted to the study of the structure of the jet in crossflow regime. It has been confirmed by experiments [1–3] and numerical studies [4, 5] that the major flow and vortical features of a typical jet in cross-flow can be represented by Figure 1.1. As shown in the figure, the flow structure consists of an orifice from which a flow is injected perpendicularly into a crossflow. The most dominant features are the counter-rotating vortex pair (CVP), a vortex structure that starts forming partly attributable to the jet shear-layer instabilities near the point of injection and takes up much of the downstream flow region, the horseshoe vortices that generates around the nozzle and wraps up the part of jet flow just issuing out from it, the shear layer vortices that result from a Kelvin-Helmholtz instability near the nozzle (more extensively studied in [2, 6, 7]) and the wake vortices that originate from the boundary layer of the wall [1].

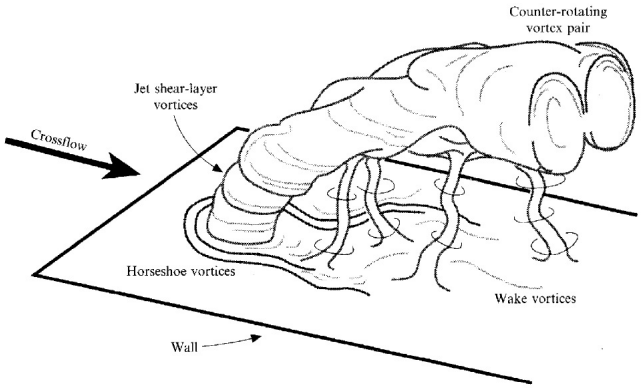

Figure 1.1: The conceptual flow and vortical features that can be identified in a jet in cross-flow. Figure adopted from [1]

Moreover, when the crossflow is supersonic, as is the case in the Scramjet configuration, some additional structures, including the bow shock formed due to the blockage of supersonic crossflow by the injected inflow, the shock train structures, and the recirculation zones generated both in the upstream and downstream vicinity of the nozzle can be observed [8].

The scramjet combustion research has been conducted in many parts of the world, both experimentally and numerically. Among them, ground and flight testings that achieve supersonic combustion were conducted and post-flight data studied at the University of Queensland [9]. A 1:1 model for the same conditions as for the flight experiment was performed by the German Aerospace Center [10]. Experiments are also carried out at the Stanford Expansion Tube Facility [8, 11, 12] to investigate the flame structure and combustion process inside a Scramjet combustion chamber. On the side of computational methods, [13] used a Reynolds-averaged Navier-Stokes solver

to study the effect of different equation of states and turbulence models. Large eddy simulation has also been a very popular approach to model turbulence [4, 14–16]. A number of combustion models including the Eddy Dissipation Concept model [17], Assumed Probability Density Function (PDF) approach [18, 19], Linear Eddy Mixing (LEM) model and the Flamele model has been proposed to characterize the turbulent combustion process. Among them, the flamelet approach and its extensions [20] based on the assumption that the flame is locally one dimensional are considered preferable in many applications due to its ability to decouple chemistry from hydrodynamics and the decrease in the computational cost comparing to traditional models. In this work, an LES solver together with an alternative combustion approach called the finite rate chemistry model is put forward and discussed in detail. The advantage of the chemistry model here is that it does not rely on the one dimensional structure assumption underlying the flamelet model. With a simpler structure and implementation effort, it allows chemistry process to be evaluated on a scale larger than the smallest scale of turbulence. The restrictions of the model are also investigated.

1.2 Dissertation Organization

The Navier-Stokes Equation that governs the fluid dynamics in general is introduced in Section 2, together with a brief discussion of the Reynolds number as a quantity that characterizes the level of turbulence of a given flow. Section 3 goes on to discuss the concepts in turbulence and the various

approaches to numerically modeling turbulent flows. Much focus is directed to the dynamic LES (Large Eddy Simulation) approach, which provides a good balance between computational cost needed and the level of resolution that could be obtained. Section 4 introduces the WENO scheme, a high-order finite volume-based numerical scheme that is applied in the Scramjet numerical simulation. The combustion models are presented in Section 5. The chemical kinetics central to the combustion process is discussed. The flame properties and structures are the major focus of a combustion model. We discusses two types of approaches to characterizing a flame, namely, the flamelet model and the finite rate chemistry. The flame resolution is studied in this section in a one-dimensional framework. Section 6 gives the results of the three-dimensional Scramjet simulation, followed by the conclusions and discussions in Section 7.

2 Governing Equations

2.1 Euler's Equations

The fundamental governing equations in fluid dynamics are the Euler's equations, which are derived from the conservation laws of mass, momentum and energy. Euler's equations characterize flows with no viscosity. It has the differential form

$$\begin{aligned} \frac{\partial \rho}{\partial t} + \frac{\partial \rho u_i}{\partial x_i} &= 0, && (2.1) \\ \frac{\partial}{\partial t}\rho u_j + \frac{\partial}{\partial x_i}\rho u_i u_j + \frac{\partial p}{\partial x_i} &= 0, && (2.2) \\ \frac{\partial \rho e}{\partial t} + \frac{\partial}{\partial x_i}(\rho u_i e) &= 0. && (2.3) \end{aligned}$$

The above equations are written using Einstein notation, in which matched pairs of indices refers to a summation.

2.2 Navier-Stokes Equations

It is assumed in Euler's equations that forces exerted on a surface of flow are normal to that surface. In other words, viscous forces are not taken into consideration. When more general fluids are considered, such an assumption becomes incorrect. A term characterizing viscous forces, the stress tensor term σ is introduced, and the more general term $-p(\vec{x},t)\mathbf{n}+\sigma(\vec{x},t)\cdot\mathbf{n}$ replaces $-p(\vec{x},t)\mathbf{n}$ in the integral form of conservation of momentum equa-

tion [21]. With a few more assumptions on the properties of σ, including it being linearly dependent on velocity gradient and being symmetric, σ can be transformed and decomposed into

$$\sigma = 2\mu[D - \frac{1}{3}(\text{div}\vec{u})I] + \zeta(\text{div}\vec{u})I. \tag{2.4}$$

Here, I is the identity matrix. μ is called the first coefficient of viscosity, and ζ the second coefficient of viscosity.

Upon further applying the divergence theorem, and leaving out the second coefficient of viscosity, the conservation of momentum equation could take on the form

$$\frac{\partial(\rho u_i)}{\partial t} + \frac{\partial}{\partial x_j}(\rho u_i u_j + p\delta_{ij} - \tau_{ij}) = 0, \tag{2.5}$$

where τ_{ij} characterizes the deviatoric stress tensor, and has the form

$$\tau_{ij} = 2\mu S_{ij}, \quad S_{ij} = \frac{1}{2}\left(\frac{\partial u_i}{\partial x_j} + \frac{\partial u_j}{\partial x_i}\right) - \frac{1}{3}\frac{\partial u_k}{\partial x_k}\delta_{ij}. \tag{2.6}$$

The Reynolds number is a very important dimensionless quantity in fluid mechanics. It is defined by the characteristic length of flow region L, the characteristic velocity U, and the coefficient $\nu = \frac{\mu}{\rho}$ of kinematic viscosity, and can be written as $Re = \frac{LU}{\nu}$. The Reynolds number can be further written as the ratio of inertia forces to viscous forces, and is often used to describe whether a given flow is laminar, transient or turbulent. A flow regime with a high Reynolds number ($Re > 4000$) indicates that viscous

forces are negligible comparing to inertial forces, and therefore the flow tends to be turbulent, as is the case of Scramjet injected flow and crossflow.

3 Turbulence Modeling

Turbulence is ubiquitous in nature and central to many applications in engineering, and is characterized by chaotic, stochastic property changes. It is also well known as the most important unsolved problem of classical physics.

It is discovered that the details of turbulence itself appear to be unpredictable, but its statistical properties are reproducible. Although the Navier-Stokes equations system is deterministic, a statistical description of turbulence is needed, especially for high-Reynolds number flow, due to the fact that fluid flows are very sensitive to changes in initial and boundary conditions, and can become unstable and irregular in time and in space.

The Russian mathematician A. N. Kolmogorov contributed a great deal in the development of turbulence research. In his 1941 work [22], later referred to as K41 theory, he made several hypotheses which laid down the framework of turbulence study afterwards. One of them is that when Reynolds number for a fluid flow is very high, small scale turbulent motions become isotropic. This is not true for flows of large scales, because the flow motions are associated with geometrical features. Isotropic small scales are the same for all turbulent flows. In addition, he postulated that this small scale is a function only of molecular viscosity ν and energy dissipation rate (per unit mass) ϵ. Since the quantity ν has dimension $[L]^2[T]^{-1}$, where $[L]$ and $[T]$ are units of length and time, respectively, and ϵ has dimension $[L]^2[T]^{-3}$, using

dimensional analysis, the scale η can be represented by $\eta = \left(\frac{\nu^3}{\epsilon}\right)^{\frac{1}{4}}$.

His other hypothesis is that at very high Reynolds numbers, all the scale statistical properties between η and L, the characteristic length of flow, can be universally and uniquely determined by r (the scale), and the energy dissipation rate ϵ.

Here, η is the so-called Kolmogorov length scale. For large scale vortices, viscous effects are not important, and kinetic energy of turbulence is mostly contained in those structures, and transferred from larger scales to smaller scales. When scales are small enough to reach the Kolmogorov length scale, molecular diffusion becomes important and viscous dissipation of energy takes place, turning kinetic energy into internal energy. In other words, in the range between characteristic length scale L of the flow and Kolmogorov length scale η, inertial effects play a much more important role than viscous effects, and it makes sense to assume that viscosity does not play a role within it. This range is called inertial range.

The way kinetic energy is distributed among different scale of turbulent flow can be characterized by the energy spectrum function $E(k)$ which satisfies

$$\int_0^\infty E(k)dk = \text{total kinetic energy}, \tag{3.1}$$

where k is the modulus of the wavevector $\mathbf{k}$ corresponding to the transformation of quantities from the physical space to the Fourier space, and the wavenumber k of a vortex of spatial dimension r is given by $k = \frac{2\pi}{r}$. There-

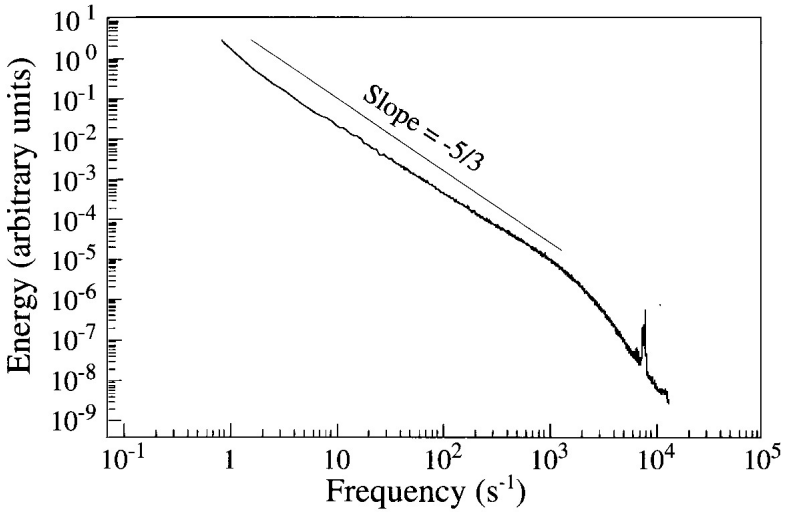

Figure 3.1: Energy spectrum in the time domain for data from S1. Reynolds number $R_\lambda = 2720$. Courtesy Y. Gagne and M. Marchand

fore, $E(k)dk$ represents the contribution to total kinetic energy of the Fourier harmonics having the absolute value of their frequency between k and $k+dk$. Using Kolmogorov's third hypothesis and dimensional analysis, in the inertial range,

$$E(k) = C\epsilon^{2/3}k^{-3/5}. \tag{3.2}$$

This is the famous $-\frac{5}{3}$ law for the energy spectrum. Figure 3.1 is one of the most famous experimental evidence that support this law, taken from [23]

3.1 Reynolds-Averaged Navier-Stokes Equations

RANS equations are time-averaged equations typically used to model turbulent flows. They involve decomposition of instantaneous variables into

its mean and fluctuation part: $u = \bar{u} + u'$. After imposing the time-averaged Reynolds operator to the governing equations, the Navier-Stokes equations can take the form [24]

$$\frac{\partial \bar{\rho}}{\partial t} + \frac{\partial \bar{\rho}\tilde{u}_j}{\partial x_j} = 0, \tag{3.3}$$

$$\frac{\partial(\bar{\rho}\tilde{u}_i)}{\partial t} + \frac{\partial}{\partial x_j}(\bar{\rho}\tilde{u}_i\tilde{u}_j) = -\frac{\partial \bar{p}}{\partial x_i} + \frac{\partial \bar{\sigma}_{ij}}{\partial x_j} - \frac{\partial(\bar{\rho}\tau_{ij})}{\partial x_j}, \tag{3.4}$$

$$\frac{\partial(\bar{\rho}\tilde{E})}{\partial t} + \frac{\partial}{\partial x_j}(\tilde{u}_j\bar{\rho}\tilde{H}) = -\frac{\partial}{\partial x_j}(\bar{q}_j + \overline{\rho E'' u_j''}). \tag{3.5}$$

Here, $\tilde{u}$ is the Favre-averaging defined for any variable u such that $\tilde{u} = \dfrac{\overline{\rho u}}{\bar{\rho}}$, and a corresponding decomposition gives $u = \bar{u} + u' = \tilde{u} + u''$. Besides, in the above equations, $\tau_{ij} = \widetilde{u_i'' u_j''}$, and

$$\bar{\sigma}_{ij} = \overline{2\mu\left(S_{ij} - \frac{1}{3}S_{kk}\delta_{ij}\right)}, \tag{3.6}$$

$$\tilde{E} = c_v\tilde{T} + \frac{\tilde{u}_i\tilde{u}_i}{2} + \frac{\widetilde{u_i'' u_i''}}{2}, \tag{3.7}$$

$$\tilde{H} = \tilde{E} + \frac{\bar{p}}{\bar{\rho}}, \tag{3.8}$$

$$\bar{q}_j = \overline{-\kappa_T \frac{\partial T}{\partial x_j}}, \tag{3.9}$$

$$\overline{\rho E'' u_j''} = c_p\bar{\rho}\widetilde{u_j'' T''} + \tilde{u}_i(\bar{\rho}\tau_{ij} - \bar{\sigma}_{ij}) + \frac{\overline{\rho u_i'' u_i'' u_j''}}{2} - \bar{\sigma}_{ij}\overline{u_i''} - \overline{\sigma_{ij}' u_i'}. \tag{3.10}$$

Terms that includes the nonlinear Reynolds stress term $\bar{\rho}\tau_{ij}$ requires further modeling efforts in order to bring a closure to the RANS equations.

3.2 Direct Numerical Simulation

Direct numerical simulation (DNS) is an approach used to solve Navier-Stokes equation without resorting to any turbulence models. Application of DNS requires that all temporal and spatial scales, from the characteristic length scale of the flow, down to the Kolmogorov scales, are to be resolved. The choice of numerical schemes is essential to the accuracy of DNS, thus low dissipation and dispersion error schemes are to be sought. Though DNS is considered to give very detailed and accurate results, the computational cost to meet the corresponding resolution requirements can be prohibitive. The cost becomes even more expensive when flows with high Reynolds number is to be simulated. It is estimated that for three-dimensional simulations, the number of operations could be proportional to as high as Re^3. Because of this, DNS is considered more as a research tool running on small-scale problems, and not suitable for solving practical engineering problems.

3.3 Large-Eddy Simulation

Large-Eddy Simulation (LES) is another class of popular approaches for simulating turbulent flows. Unlike RANS, the flow field is resolved down to a certain length scale, and solved via filtered Navier-Stokes Equations. Scales smaller than that are called subgrid scales. These scales are eliminated from the governing equations, and they are modeled rather than resolved. The resolved scales are usually much larger than the Kolmogorov scale, therefore

making LES much more manageable computationally than DNS, and generally has a complexity in between DNS and RANS. LES involves separating velocity field into resolved and sub-grid components. The resolved part is a filtered field, and the filtering operation can be defined generally in terms of a convolution against a kernel F

$$\bar{u} = F * u \tag{3.11}$$

where u is a flow field variable. Among different filtering operations, a density-weighted Favre filtering is widely used, with the purpose of avoiding modeling the mass concentration equation and simplify the resulting equation system. For an arbitrary quantity q, Favre filtering is defined as $\widetilde{q} = \dfrac{\overline{\rho q}}{\overline{\rho}}$.

After applying this filter, the Navier-Stokes equations have the following form

$$\begin{aligned}
\frac{\partial \overline{\rho}}{\partial t} + \frac{\partial \overline{\rho}\widetilde{u_i}}{\partial x_i} &= 0, && (3.12)\\
\frac{\partial \overline{\rho}\widetilde{u_i}}{\partial t} + \frac{\partial \overline{\rho}\widetilde{u_i}\widetilde{u_j}}{\partial x_j} &= -\frac{\partial \overline{p}}{\partial x_i} + \frac{\partial \overline{\sigma_{ij}}}{\partial x_j} - \frac{\partial \tau_{ij}}{\partial x_i}, && (3.13)\\
\frac{\partial \overline{E}}{\partial t} + \frac{\partial (\overline{E}+\overline{p})\widetilde{u_j}}{\partial x_j} &= \frac{\partial \overline{d_{ij}}\widetilde{u_i}}{\partial x_j} + \frac{\partial}{\partial x_j}\left(\overline{\kappa}\frac{\partial \widetilde{T}}{\partial x_j}\right) + \frac{\partial}{\partial x_j}\left((\widetilde{H_h} - \widetilde{H_l})\overline{\rho}\widetilde{D}\frac{\partial \widetilde{\psi}}{\partial x_j}\right) \\
&\quad + \left(\frac{1}{2}\frac{\partial \tau_{kk}\widetilde{u_j}}{\partial x_j} - \frac{\partial q_j^{(H)}}{\partial x_j} - \frac{\partial q_j^{(T)}}{\partial x_j} - \frac{\partial q_j^{(V)}}{\partial x_j}\right), && (3.14)\\
\frac{\partial \overline{\rho}\widetilde{\psi}}{\partial t} + \frac{\partial \overline{\rho}\widetilde{\psi}\widetilde{u_j}}{\partial x_j} &= \frac{\partial}{\partial x_j}\left(\overline{\rho}\widetilde{D}\frac{\partial \widetilde{\psi}}{\partial x_j}\right) - \frac{\partial q_j^{(\psi)}}{\partial x_j}, && (3.15)
\end{aligned}$$

where the Subgrid Scale terms are expressed as

$$\tau_{ij} = \overline{\rho}(\widetilde{u_i u_j} - \widetilde{u}_i \widetilde{u}_j), \tag{3.16}$$

$$q_j^{(H)} = \overline{\rho}(\widetilde{c_p T u_j} - \widetilde{c_p} \widetilde{T} \widetilde{u}_j), \tag{3.17}$$

$$q_j^{(T)} = \frac{1}{2}\overline{\rho}(u_k \widetilde{u_k u_j} - \widetilde{u}_k \widetilde{u}_k \widetilde{u}_j), \tag{3.18}$$

$$q_j^{(V)} = \overline{\sigma_{ij} u_i} - \overline{\sigma_{ij}} \widetilde{u}_i, \tag{3.19}$$

$$q_j^{(\psi)} = \overline{\rho}(\widetilde{\psi u_j} - \widetilde{\psi} \widetilde{u}_j), \tag{3.20}$$

and the filtered variables are expressed as

$$\overline{E} = \overline{\rho}\widetilde{e} + \frac{\overline{\rho}\widetilde{v_k}^2}{2} + \frac{\tau_{kk}}{2}, \tag{3.21}$$

$$\widetilde{H_h} = \widetilde{e_h} + \frac{\overline{p}}{\overline{\rho}}, \tag{3.22}$$

$$\widetilde{H_l} = \widetilde{e_l} + \frac{\overline{p}}{\overline{\rho}}. \tag{3.23}$$

Here, $\overline{E}$, $\widetilde{H_h}$ and $\widetilde{H_l}$ stand for total specific energy and partial specific enthalpy of two species, respectively.

3.3.1 Dynamic Smagorinsky Model

After the equations are modified and variables all transformed into filtered quantities, the next step is to model those SGS terms left in these equations. The term τ_{ij} that appears in momentum equations, which is also known as SGS stress tensor is the first crucial term, and the only one that needs to be

modeled in order to close the momentum equation.

This term can be separated into a trace-free term and an isotropic term

$$\tau_{ij} = \tau_{ij}^a + \tau_{ij}^i = \left(\tau_{ij} - \tau_{kk}\frac{\delta_{ij}}{3}\right) + \tau_{kk}\frac{\delta_{ij}}{3}. \tag{3.24}$$

For incompressible flows, only the anisotropic tensor is relevant since the isotropic part is absorbed into the pressure; for compressible flows on the other hand, both terms should be considered. With the trace-free Smagorinsky eddy viscosity model,

$$\tau_{ij}^a = \tau_{ij} - \tau_{kk}\frac{\delta_{ij}}{3} = -2C_S\overline{\rho}\Delta^2|\widetilde{S}|(\widetilde{S}_{ij} - \frac{1}{3}\widetilde{S}_{kk}\delta_{ij}), \tag{3.25}$$

where $\widetilde{S}_{ij} = \frac{1}{2}\left(\frac{\partial\widetilde{u}_i}{\partial x_j} + \frac{\partial\widetilde{u}_j}{\partial x_i}\right)$ and $|\widetilde{S}| = \sqrt{2\widetilde{S}_{ij}\widetilde{S}_{ij}} = \sqrt{\sum 2\widetilde{S}_{ij}^2}$, and Δ is the filter width. With Yoshizawa's expression,

$$\tau_{ij}^i = \tau_{kk}\frac{\delta_{ij}}{3} = \frac{2}{3}\delta_{ij}C_I\Delta^2\overline{\rho}|\widetilde{S}|^2. \tag{3.26}$$

Therefore, the modeled subgrid scale (SGS) stress τ_{ij} is

$$\tau_{ij}^M = -2C_S\overline{\rho}\Delta^2|\widetilde{S}|(\widetilde{S}_{ij} - \frac{1}{3}\widetilde{S}_{kk}\delta_{ij}) + \frac{2}{3}\delta_{ij}C_I\Delta^2\overline{\rho}|\widetilde{S}|^2. \tag{3.27}$$

In order to close the momentum equation, firstly, using Favre-filtering

relation, τ_{ij} can be further written as

$$\tau_{ij} = \overline{\rho}(\widetilde{u_i u_j} - \widetilde{u}_i \widetilde{u}_j) = \overline{\rho u_i u_j} - \frac{\overline{\rho u_i}\ \overline{\rho u_j}}{\overline{\rho}}. \tag{3.28}$$

In the dynamic SGS model, the central idea is the introducion of a test filter which is larger than the resolved grid filter (in current Scramjet problem, it is set to be two times the dimension of the original grid filter, but in fact can be chosen at will) so that the data information can be utilized. The filter width of the test filter is denoted by $\widehat{\Delta}$. The test filter is always applied to the resolved field, and on this filter, a stress term similar to the form of τ_{ij} can be defined as follows

$$T_{ij} = \widehat{\overline{\rho u_i u_j}} - \frac{\widehat{\overline{\rho u_i}}\,\widehat{\overline{\rho u_j}}}{\widehat{\overline{\rho}}}. \tag{3.29}$$

With Germano's Identity [25], the Leonard stress tensor L_{ij} is expressed in terms of T_{ij} and τ_{ij}

$$\begin{aligned} L_{ij} = T_{ij} - \widehat{\tau}_{ij} &= \widehat{\overline{\rho u_i u_j}} - \frac{\widehat{\overline{\rho u_k}}\,\widehat{\overline{\rho u_j}}}{\widehat{\overline{\rho}}} - \left(\widehat{\overline{\rho u_i u_j}} - \left(\frac{\widehat{\overline{\rho u_i}\ \overline{\rho u_j}}}{\overline{\rho}} \right) \right) && (3.30) \\ &= \left(\frac{\widehat{\overline{\rho u_i}\ \overline{\rho u_j}}}{\overline{\rho}} \right) - \frac{\widehat{\overline{\rho u_k}}\,\widehat{\overline{\rho u_j}}}{\widehat{\overline{\rho}}} && (3.31) \\ &= \widehat{\overline{\rho}\widetilde{u}_i \widetilde{u}_j} - \frac{\widehat{\overline{\rho}\widetilde{u}_i}\,\widehat{\overline{\rho}\widetilde{u}_j}}{\widehat{\overline{\rho}}}. && (3.32) \end{aligned}$$

The Leonard stress is totally resolved, while the other two stress tensors in

this relation, T_{ij} and $\widehat{\tau}_{ij}$ are both modeled using the trace-free Smagorinsky eddy viscosity model, and we obtain the following relation

$$L_{ij}^a = T_{ij}^a - \widehat{\tau}_{ij}^a = 2C_S\Delta^2\overline{\rho}\widehat{\widetilde{|S|}\widetilde{S}_{ij}^a} - 2C_S\widehat{\Delta}^2\widehat{\overline{\rho}}\widehat{\widetilde{|S|}\widetilde{S}}_{ij}^a = C_S M_{ij}^a, \tag{3.33}$$

where

$$M_{ij}^a = 2\Delta^2\overline{\rho}\widehat{\widetilde{|S|}\widetilde{S}_{ij}^a} - 2\widehat{\Delta}^2\widehat{\overline{\rho}}\widehat{\widetilde{|S|}\widetilde{S}}_{ij}^a. \tag{3.34}$$

The above equation is actually an overdetermined system of equations which corresponds to five (off-diagonal components of stress matrix) relations between M_{ij}^a and L_{ij}^a. In order to give an approximate solution for C_S, the most common way is via least-square method. When a target region is chosen (details explained below), an average over variables M_{ij}^a and L_{ij}^a within this region is applied and the resulting formula for C_S becomes

$$C_S = \frac{\langle(\sum L_{ij}^a M_{ij}^a)^+\rangle}{\langle(\sum M_{ij}^a M_{ij}^a)^+\rangle}. \tag{3.35}$$

Here, the expression $(...)^+$ means only positive terms are added up, and negative terms are ignored. The expression $\langle ...\rangle$ indicates the averaging process.

In order to determine coefficient C_I, a similar process leads to the expression

$$L_{kk}^i = T_{kk}^i - \hat{\tau}_{kk}^i = -2C_I\Delta^2\widehat{\overline{\rho}|\widetilde{S}|^2} + 2C_I\hat{\Delta}^2\hat{\overline{\rho}}|\hat{\widetilde{S}}|^2 = C_I M_{kk}^i \tag{3.36}$$

$$M_{kk}^i = -2\Delta^2\widehat{\overline{\rho}|\widetilde{S}|^2} + 2\hat{\Delta}^2\hat{\overline{\rho}}|\hat{\widetilde{S}}|^2. \tag{3.37}$$

Similar to the above treatment, since this relation corresponds to three (diagonal components of stress matrix) equations, an averaging over a specified area leads to the least-square type of solution of C_I in the form of

$$C_I = \frac{\langle L^i_{kk} \rangle}{\langle M^i_{kk} \rangle}. \tag{3.38}$$

In the energy equation, among the three sub-grid terms $q_j^{(H)}$, $q_j^{(T)}$ and $q_j^{(V)}$, the heat transport flux $q_j^{(H)}$ is the one with the lowest order, and the only one considered here in the modeling process. ($q_j^{(T)}$ and $q_j^{(V)}$ are set to be zero). Heat transport flux is modeled as

$$q_i^{(H)M} = -\bar{\rho}\tilde{c}_p \frac{C_S \Delta^2 |\tilde{S}|}{\mathrm{Pr_t}} \frac{\partial \tilde{T}}{\partial x_i} = -\frac{\tilde{c}_p \nu_t}{\mathrm{Pr_t}} \frac{\partial \tilde{T}}{\partial x_i} = -\kappa_t \frac{\partial \tilde{T}}{\partial x_i}, \tag{3.39}$$

where $\mathrm{Pr_t}$ is the Prandtl number and the one to be determined by the dynamic model in a similar fashion.

Applying Favre filtering to the flux term gives

$$Q_i^{(H)} = \widehat{\overline{\rho c_p T v_i}} - \frac{\widehat{\overline{\rho c_p}}\,\widehat{\overline{\rho T}}\,\widehat{\overline{\rho v_i}}}{\widehat{\overline{\rho}}^2}, \tag{3.40}$$

and is modeled by

$$Q_i^{(H)M} = -\hat{\bar{\rho}}\hat{\tilde{c}}_p \frac{C_S \hat{\Delta}^2 |\hat{\tilde{S}}|}{\mathrm{Pr_t}} \frac{\partial \hat{\tilde{T}}}{\partial x_i}. \tag{3.41}$$

Germano's identity again gives rise to the following relation

$$L_i^{(H)} = Q_i^{(H)} - \widehat{q_i^{(H)}} = \left(\frac{\widehat{\overline{\rho c_p}\,\overline{\rho T}\,\overline{\rho v_i}}}{\bar{\rho}^2} \right) - \frac{\widehat{\overline{\rho c_p}}\,\widehat{\overline{\rho T}}\,\widehat{\overline{\rho v_i}}}{\hat{\bar{\rho}}^2} = \bar{\rho}\widehat{\tilde{c}_p \tilde{T}}\tilde{v}_i - \frac{\widehat{\bar{\rho}\tilde{c}_p}\,\widehat{\bar{\rho}\tilde{T}}\,\widehat{\bar{\rho}\tilde{v}_i}}{\hat{\bar{\rho}}^2}. \quad (3.42)$$

Eddy diffusivity SGS model for Pt gives

$$L_i^{(H)} = Q_i^{(H)M} - \widehat{q_i^{(H)M}} = \frac{C_S}{\mathrm{Pr}} \left(\Delta^2 \left(\bar{\rho}\tilde{c}_p \widehat{|\tilde{S}|\frac{\partial \tilde{T}}{\partial x_i}} \right) - \hat{\Delta}^2 \hat{\bar{\rho}}\hat{\tilde{c}}_p |\hat{\tilde{S}}| \frac{\partial \hat{\tilde{T}}}{\partial x_i} \right) = \frac{C_S}{\mathrm{Pr}} M_i^{(H)}, \quad (3.43)$$

where

$$M_i^{(H)} = \Delta^2 \left(\bar{\rho}\tilde{c}_p \widehat{|\tilde{S}|\frac{\partial \tilde{T}}{\partial x_i}} \right) - \hat{\Delta}^2 \hat{\bar{\rho}}\hat{\tilde{c}}_p |\hat{\tilde{S}}| \frac{\partial \hat{\tilde{T}}}{\partial x_i}. \quad (3.44)$$

Again, a least-square approach is applied to the system of three equations and the $\mathrm{Pr_t}$ is calculated as

$$\mathrm{Pr}_t = C_S \frac{\langle (\sum M_i^{(H)} M_i^{(H)})^+ \rangle}{\langle (\sum L_i^{(H)} M_i^{(H)})^+ \rangle}. \quad (3.45)$$

Lastly, we model the term $q_j^{(\psi)}$ in species concentration equations and derive the Schmidt number $\mathrm{Sc_t}$ dynamically. The linear gradient assumption leads to

$$q_i^{(\psi)M} = -\rho \frac{C_S \Delta^2 |\tilde{S}|}{\mathrm{Sc_t}} \frac{\partial \tilde{\psi}}{\partial x_i}. \quad (3.46)$$

At test filter grid level,

$$Q_i^{(\psi)} = \widehat{\overline{\rho v_i \psi}} - \frac{\widehat{\overline{\rho v_i}}\,\widehat{\overline{\rho \psi}}}{\hat{\bar{\rho}}}. \quad (3.47)$$

$Q_i^{(\psi)}$ is modeled by

$$Q_i^{(\psi)M} = -\hat{\bar{\rho}}\frac{C_S\hat{\Delta}^2|\hat{\tilde{S}}|}{\mathrm{Sc_t}}\frac{\hat{\tilde{\psi}}}{\partial x_i}. \tag{3.48}$$

Using Germano's identity again

$$L_i^{\psi} = Q_i^{(\psi)} - \widehat{q_i^{(\psi)}} = \left(\frac{\widehat{\overline{\rho v_i}\overline{\rho\psi}}}{\bar{\rho}}\right) - \frac{\widehat{\overline{\rho v_i}}\widehat{\overline{\rho\psi}}}{\hat{\bar{\rho}}} = \widehat{\bar{\rho}\tilde{v}_i\tilde{\psi}} - \frac{\widehat{\bar{\rho}\tilde{v}_i}\widehat{\bar{\rho}\tilde{\psi}}}{\hat{\bar{\rho}}}. \tag{3.49}$$

The modeled quantity is

$$L_i^{\psi} = Q_i^{(\psi)M} - \widehat{q_i^{(\psi)M}} = \frac{C_S}{\mathrm{Sc_t}}\left(\Delta^2\left(\widehat{\bar{\rho}|\tilde{S}|\frac{\partial\tilde{\psi}}{\partial x_i}}\right) - \hat{\Delta}^2\hat{\bar{\rho}}|\hat{\tilde{S}}|\frac{\partial\hat{\tilde{\psi}}}{\partial x_i}\right) = \frac{C_S}{\mathrm{Sc_t}}M_i^{(\psi)}, \tag{3.50}$$

where

$$M_i^{(\psi)} = \Delta^2\left(\widehat{\bar{\rho}|\tilde{S}|\frac{\partial\tilde{\psi}}{\partial x_i}}\right) - \hat{\Delta}^2\hat{\bar{\rho}}|\hat{\tilde{S}}|\frac{\partial\hat{\tilde{\psi}}}{\partial x_i}. \tag{3.51}$$

The modeled Schmidt number $\mathrm{S_{Ct}}$ is thus calculated via least-square approach

$$\mathrm{Sc}_t = C_S\frac{\langle(\sum M_i^{(\psi)}M_i^{(\psi)})^+\rangle}{\langle(\sum L_i^{(\psi)}M_i^{(\psi)})^+\rangle}. \tag{3.52}$$

3.3.2 Averaging Procedure

Before least-square approach, the dynamic SGS model used in the previous section to derive the expression of the eddy viscosity coefficients, the Prandtl number and the Schmidt number are all functions of time and space. In various applications, however, it is shown that the the right-hand side of

the fitting equation could become zero in some cells. In order for the model to be consistent and well conditioned, the coefficients in question are commonly averaged over a specified region in the flow. The way to determine the appropriate area of averaging is problem specific, and is usually dependent on the properties of the flow. The concept of statistical homogeneity of flow is introduced, and it is assumed that coefficients C_S, C_I, Pr and Sc are independent in the homogeneous directions of the flow [26]. Therefore, an averaging procedure can be applied along the homogenous direction to adjust the values of coefficients away from zero. In the context of Rayleigh-Taylor instability problems, for example, a certain level of homogeneity exists on all points in space with the same z-coordinate, and therefore, planar average could be applied on the dynamically calculated coefficients. For the 3D Richtmyer-Meshkov instability problem with a circular geometry, on the other hand, a spherical average is usually employed. In the case of Scramjet simulation, however, the complexities of flow on many scales means that a homogeneous direction may not exist after all. Therefore, the model is further adapted so that the region upon which to apply averaging is restricted to small mesh blocks whose dimensions are left to choice, called localized mesh block averaging. The advantage of this adaptive SGS model is that it no longer involves data transfer and communications among processors, which could be a bottleneck for either planar or spherical averaging. The freedom to choose the size of averaging mesh blocks also makes the model more flexible and attractive to use. Figure 3.2 illustrates the effect of local

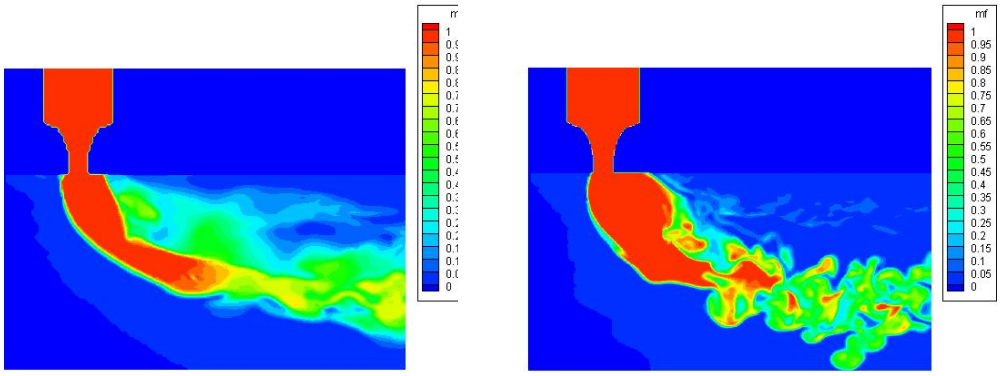

Figure 3.2: H_2 concentration profile outside of nozzle for 240 micron (left) and 120 micron (right), using local averaging procedure.

averaging procedure on the Scramjet simulation with two grid levels.

3.3.3 Traditional Smagorinsky Model

Comparing to the dynamic version of the sub-grid model described in the above section, the traditional Smagorinsky model [27] assumes the eddy viscosity coefficients are constant, and should be chosen differently for different flow fields. Moreover, there are some other restrictions. According to [26], (i) the model does not have the correct limiting behavior near the wall; (ii) the model does not vanish in laminar flow, and it is demonstrated to be too dissipative in the laminar-turbulent transition region; (iii) the model does not account for backscatter of energy from small scales to large scales, which has been shown to be of importance in the transition regime; (iv) compressibility effects are not included in the model. Dynamic SGS model, based on the application of Smagorinsky model at two different filter level, is therefore

developed to overcome some of those drawback, and produce more accurate simulation results. However, the Smagorinsky model is still widely applied in many large eddy simulation problems due to its simplicity and effectiveness in many applications.

4 Numerical Methods

4.1 Finite Volume Approach

The finite volume approach is a numerical method based on the integral form of a PDE. It is well suited as a numerical scheme to describe physical properties of flows. Conservation laws are a very important class of homogeneous hyperbolic partial differential equations, and they are usually derived directly from physical laws. A one-dimensional conservation law has the form

$$U_t(x,t) + f(U(x,t))_x = 0. \tag{4.1}$$

Here, $f(U(x,t))$ is called the flux function, and U is an unknown function, usually a certain flow quantity. Let $x_j = j\Delta x$, Equation 4.1 can be further written into an integral form over an interval $[x_j - \frac{1}{2}\Delta x, x_j + \frac{1}{2}\Delta x]$

$$\frac{d}{dt}\int_{x_j-\frac{1}{2}\Delta x}^{x_j+\frac{1}{2}\Delta x} U(x_j,t) = f\left(U\left(x_j - \frac{1}{2}\Delta x, t\right)\right) - f\left(\left(U(x_j + \frac{1}{2}\Delta x, t\right)\right). \tag{4.2}$$

Let $q_j = \frac{1}{\Delta x}\int_{x_j-\frac{1}{2}\Delta x}^{x_j+\frac{1}{2}\Delta x} f(U(x,t))dx$, and averaging over $[t_i, t_i + \Delta t]$ gives

$$\frac{q_j^{t_i+\Delta t} - q_j^{t_i}}{\Delta t} = \frac{1}{\Delta t}\int_{t_i}^{t_i+\Delta t} f(U(x_j - \frac{1}{2}\Delta x, t))dt - \frac{1}{\Delta t}\int_{t_i}^{t_i+\Delta t} f(U(x_j + \frac{1}{2}\Delta x, t))dt. \tag{4.3}$$

Let $F^i_{j-\frac{1}{2}} = \int_{t_i}^{t_i+\Delta t} f(U(x_j - \frac{1}{2}\Delta x, t))dt$, after rearranging

$$q_j^{t_i+\Delta t} = q_j^{t_i} - \frac{\Delta t}{\Delta x}(F^i_{j+\frac{1}{2}} - F^i_{j-\frac{1}{2}}). \tag{4.4}$$

If we can approximate the average flux $F^i_{j-\frac{1}{2}}$ and $F^i_{j+\frac{1}{2}}$, we obtain a discrete numerical scheme. The choice of this numerical flux function defines various forms of finite volume schemes.

4.2 WENO Scheme

The WENO scheme is a high-resolution finite volume scheme developed to combine stencils of lower orders to reach a higher order approximation. It extends the ENO scheme which selects a single candidate stencil only. WENO scheme uses a convex combination of all candidate stencils, and each one is given a weight that corresponds to the contribution of that stencil to the total numerical flux. The weights are defined so that away from flow discontinuities, it approaches certain optimal weights in order to get a higher order accuracy; in regions of discontinuities and shocks on the other hand, the stencils that include the discontinuous points are assigned a near zero weight.

In the following, a 5^{th} order flux approximation of the WENO scheme is described, largely following the derivation of [28]. The scheme is the one being used in Scramjet simulation to achieve a high order approximation of

complicated flow structures. The flux approximation can be expressed as

$$\hat{f} = \sum_{k=0}^{2} w_k h_k(f_{-2}, f_{-1}, f_0), \tag{4.5}$$

where h_k are simply linear combinations of fluxes within the stencil k, and can be expressed as $h_k(f_{-2}, f_{-1}, f_0) = \sum_{j=0}^{2} a_{k,j} h_{j-2}$.

For stability purposes, the approach described below are applied to f^+ and f^- respectively, where f^+ and f^- are the positive and negative components corresponding to flux splitting $f(x) = f^+(x) + f^-(x)$, where $\frac{d}{dx} f^+(x) \geq 0$, and $\frac{d}{dx} f^-(x) \leq 0$. The Lax-Friedrichs flux splitting is the one commonly used, and has the following form

$$f^{\pm}(x) = \frac{1}{2}(f(x) \pm ax), \tag{4.6}$$

where a is chosen to be the global maximum of $|f'(x)|$.

For a system of equations, the WENO scheme and the corresponding weights of candidate stencils are computed in the local characteristic fields. The Jacobian matrices are evaluated at the average mean values of state variables of two neighboring cells. Denote $\mathbf{l}_i$ and $\mathbf{r}_i$ as the left and right eigenvectors of the Jacobian matrix J_i at local characteristic field i, respectively. The approximation of flux in the mapped field can therefore be replaced by

$$\tilde{f}_i = \sum_{k=0}^{2} \tilde{w}_k \tilde{h}_k, \tag{4.7}$$

Table 4.1: Coefficients $a^r_{k,l}$ (left) and C^r_k (right)

r	k	$l=0$	$l=1$	$l=2$
3	0	1/3	−7/6	11/6
	1	−1/6	5/6	1/3
	2	1/3	5/6	−1/6

C^r_k	$k=0$	$k=1$	$k=2$
$r=2$	1/3	2/3	-
$r=3$	1/10	6/10	3/10

where $\tilde{w}_k = w_k(\mathbf{l}_i\cdot\mathbf{f}_{-2}, \mathbf{l}_i\cdot\mathbf{f}_{-1}, \mathbf{l}_i\cdot\mathbf{f}_0, \mathbf{l}_i\cdot\mathbf{f}_1, \mathbf{l}_i\cdot\mathbf{f}_2)$ and $\tilde{h}_k = h_k(\mathbf{l}_i\cdot\mathbf{f}_{k-2}, \mathbf{l}_i\cdot\mathbf{f}_{k-1}, \mathbf{l}_i\cdot\mathbf{f}_k)$ at stencil k. $\tilde{w}_k$ is defined by

$$w_k = \frac{\alpha_k}{\alpha_0 + \alpha_1 + \alpha_2}, \tag{4.8}$$

where

$$\alpha_k = \frac{C^r_k}{(\epsilon + IS_k)^p}, \quad k = 0, 1, 2 \tag{4.9}$$

and IS_k, $(k = 0, 1, 2)$ are evaluated to be

$$IS_0 = \frac{13}{12}(f_{-2} - 2f_{-1} + f_0)^2 + \frac{1}{4}(f_{-2} - 4f_{-1} + 3f_0)^2, \tag{4.10}$$

$$IS_1 = \frac{13}{12}(f_{-1} - 2f_0 + f_1)^2 + \frac{1}{4}(f_{-1} - f_1)^2, \tag{4.11}$$

$$IS_2 = \frac{13}{12}(f_0 - 2f_1 + f_2)^2 + \frac{1}{4}(3f_0 - 4f_1 + f_2)^2. \tag{4.12}$$

C^r_k is given in Table 4.1, ϵ is a small positive value introduced to avoid the denominators of α_k being zero. The power p is chosen to be 2 as [28] suggests.

Fluxes $\tilde{f}$ are then mapped back to the spatial field by

$$\hat{f} = \sum_{i=1}^{m} \tilde{f}_i \mathbf{r}_i \tag{4.13}$$

using right eigenvectors of J_i.

The time discretization $L(U) = \dfrac{q_j^{i+1}(U) - q_j^i(U)}{\Delta t}$ is approximated by a 3^{th} order TVD Runge-Kutta scheme expressed by

$$U^0 = U^n + \Delta t L(U^n), \tag{4.14}$$

$$U^1 = \frac{3}{4}U^n + \frac{1}{4}U^{(1)} + \frac{1}{4}\Delta t L(U^1), \tag{4.15}$$

$$U^{n+1} = \frac{1}{3}U^n + \frac{2}{3}U^{(2)} + \frac{2}{3}\Delta t L(U^{(2)}). \tag{4.16}$$

5 Combustion Models and Mesh Resolution Analysis

5.1 Thermodynamic Properties and Equations of State

The interactions among reacting species in both hydrodynamic and combustion process call for an accurate description of their thermodynamic properties and multi species equations of state. Most formulas and results presented in this section are widely used in the thermodynamics community, and can be found in standard references [29–31], For simulation purposes, these equations of state and thermodynamic relations are implemented and grouped into a library separate from the hydrodynamic part of scheme to allow for fast access from the hydro code.

The theory of thermodynamics [32] indicates that for any given medium, only two of the parameters P, T, V, E and S are independent. A fundamental relation in thermodynamic theory (derived from the first and second law in thermodynamics) involves the change in internal energy. To be more specific, a change in the internal energy in a portion of medium is the sum of the work done on the medium in the form of pressure, plus the heat transferred to the medium. This fact is often expressed as

$$dE = TdS - PdV, \quad P(S,V) = -\left.\frac{\partial E}{\partial V}\right|_S, \quad T(S,V) = \left.\frac{\partial E}{\partial S}\right|_V.$$

Another fundamental thermodynamic property of a flow is that, given constant entropy, the pressure increases with increasing density, or in functional form, $P = F(\rho, S)$. This relation leads to a convenient definition of a positive quantity $c^2 = \dfrac{\partial P}{\partial \rho} = F_\rho(\rho, S)$. The quantity c is the well known sound speed.

The equation of state is a set of equations that describes the relationship between thermodynamic state variables under given physical conditions. Two very common and closely related classes of equation of state for a single species are the ideal gas and a one parameter family of ideal gases, the gamma-law gas.

An ideal gas is a medium that satisfies the law of Boyle and Gay-Lussac, and can be written in the form

$$PV = \frac{RT}{M}, \tag{5.1}$$

where R is the universal gas constant, and M is the molecular weight of the gas. A very important feature of an ideal gas is that the internal energy is a function of temperature only, or $E = E(T)$. A gamma-law gas further assumes that the internal energy is simply proportional to the temperature, and can be written as $E = C_V T$, where constant C_V is the specific heat at constant volume. When a gas is assumed to be a gamma-law gas, further derivation shows that

$$P = P(\rho, S) = A(S)\rho^\gamma. \tag{5.2}$$

Here, $A(S)$ is a function of entropy alone, and γ is called adiabatic exponent,

and is a constant commonly lying within the range $1 \leq \gamma \leq \frac{5}{3}$. Moderate-temperature air, which is a mixture of gases, has a value of about $\gamma = 1.4$.

Further derivation shows that γ can be written as a ratio of two quantities, the specific heat at constant pressure C_P and the specific heat at constant volume C_V: $\gamma = \dfrac{C_P}{c_V}$. The two quantities are defined by

$$C_V = T \left.\frac{\partial S}{\partial T}\right|_V \quad \text{and} \quad C_P = T \left.\frac{\partial S}{\partial T}\right|_P, \tag{5.3}$$

and related by the identity $C_P - C_V = R/M$.

In the Scramjet simulations, the assumption of an ideal gas is adopted, and the quantities C_P, H, S can be written as functions of T, so that $C_P = C_P(T)$, $H = H(T)$ and $S = S(T)$. For simulation purposes, polynomial approximations are derived for thermodynamic properties and transport coefficients of a great number of gaseous species, and least-square fitting to experimental measurements are used to calculate polynomial coefficients. NASA provides tables of these coefficients [33] that fits a fourth-order polynomial to the dimensionless quantity $\dfrac{C_P(T)}{R}$ for individual species, and further derives functional forms of $H(T)$ and $S(T)$ via integration as follows

$$\frac{C_P}{R} = a_1 + a_2 T + a_3 T^2 + a_4 T^3 + a_5 T^4 \tag{5.4}$$

$$\frac{H}{RT} = a_1 + a_2 \frac{T}{2} + a_3 \frac{T^2}{3} + a_4 \frac{T^3}{4} + a_5 \frac{T^4}{5} + \frac{a_6}{T} \tag{5.5}$$

$$\frac{S}{R} = a_1 \ln T + a_2 T + a_3 \frac{T^2}{2} + a_4 \frac{T^3}{3} + a_5 \frac{T^4}{4} + a_7. \tag{5.6}$$

To improve the table accuracy, the temperature range is divided into the lower part, from 300K to 1000K, and the higher part, from 1000K to 5000K. The fitting requires that the two sets of coefficients have the common values at the joining point $T = 1000$K.

In Scramjet numerical modeling, the internal energy E and the density ρ are known quantities, and the pressure P is needed to close the hydrodynamic equations. The temperature T should be determined for the chemistry calculation. This is done using a nonlinear equation solver, which is derived using the expressions

$$P = (\gamma(T) - 1)\rho E, \qquad \frac{P}{\rho} = \frac{RT}{M}, \tag{5.7}$$

$$\gamma = \frac{C_P}{c_V}, \qquad C_P - C_V = \frac{R}{M}. \tag{5.8}$$

Therefore,

$$\frac{RT}{M} = \frac{P}{\rho} = (\gamma(T) - 1)E = \left(\frac{C_P}{C_P - R/M} - 1\right) E. \tag{5.9}$$

When written explicitly in terms of T

$$\frac{RT}{M} = \left(\frac{a_1 + a_2T + a_3T^2 + a_4T^3 + a_5T^4}{a_1 + a_2T + a_3T^2 + a_4T^3 + a_5T^4 - 1/M} - 1\right) E. \tag{5.10}$$

Further simplifications give

$$(a_1 + a_2T + a_3T^2 + a_4T^3 + a_5T^4 - 1/M)RT = E. \tag{5.11}$$

The last equation is solved with respect to T with root-finding algorithms.

For a single species, using kinetic theory, the individual μ_i and λ_i are modeled as [31, 34]

$$\mu_k = 2.6693 \times 10^{-5} \frac{\sqrt{M_k T}}{{\sigma_k}^2 {\Omega_k}^{(2,2)}}, \tag{5.12}$$

$$\lambda_k = \mu_k \left(C_{Pk} + \frac{5}{4} \frac{R}{M_k} \right). \tag{5.13}$$

$\Omega_k^{(2,2)}$ is called the collision integral. It is a function of the reduced temperature T_r, defined as the ratio of the actual temperature divided by the critical temperature, and is confirmed by experimental data to have the following empirical expression

$$\begin{aligned} {\Omega_k}^{(2,2)} &= \exp[0.45667 - 0.53955 \ln(T_r) + 0.18265 (\ln(T_r))^2 - \\ &\quad 0.03629 (\ln(T_r))^3 + 0.00241 (\ln(T_r))^4]. \quad (1 < T_r < 90) \end{aligned} \tag{5.14}$$

For a mixture of N ideal gases, the total pressure is the sum of partial pressures of individual gases according to Dalton's law

$$p = \sum_{k=1}^{N} p_k, \quad \text{in which } p_k = \rho_k \frac{R}{M_k} T. \tag{5.15}$$

Here, p_k, ρ_k and M_k stand for partial pressure, partial density, and molecular weight of individual gases. Since the total density is the sum of the partial

density of the individual species,

$$\rho = \sum_{k=1}^{N} \rho_k \tag{5.16}$$

the average molecular weight of the mixture can be evaluated as

$$M = \frac{1}{\sum_{k=1}^{N} \frac{Y_k}{M_k}}, \tag{5.17}$$

where $Y_k = \dfrac{m_k}{m}$ stands for mass fraction of species k, m_k is the mass of species k in a given volume, and m is the total mass in that volume. A mixture of γ law gases is still a γ law gas. According to the derivation in [35], the mixture $\gamma(T)$ can be expressed as a combination of individual gamma-law gases

$$\frac{1}{\gamma(T)-1} = M \sum_{k=1}^{N} \frac{1}{(\gamma_i(T)-1)} \frac{Y_k}{M_k}, \tag{5.18}$$

where $\gamma_i(T)$ is the value of gamma of species i.

The dynamic viscosity and thermal conductivity of the gas mixture are calculated empirically based on averages of the individual species properties [36]

$$\mu = \sum_{k=1}^{N} \frac{Y_k \mu_k}{\Delta_k}, \quad \lambda = \sum_{k=1}^{N} \frac{Y_k \lambda_k}{\Delta_k}. \tag{5.19}$$

Here

$$\triangle_k = \sum_{k=1}^{N} G_{kl} \frac{M_k}{M_l} Y_l, \tag{5.20}$$

and

$$G_{kl} = \frac{1}{\sqrt{8}} \left(1 + \frac{M_k}{M_l}\right)^{-1/2} \left[1 + \left(\frac{\mu_k}{\mu_l}\right)^{-1/2} \left(\frac{M_l}{M_k}\right)^{1/4}\right]^2 . \tag{5.21}$$

5.2 Chemical Kinetic Mechanism

Detailed chemistry is the starting point for the calculation of combustion processes. The detailed chemistry for H_2 combustion includes 21 reversible elementary reactions [37]. This mechanism is widely accepted and found to be in good agreement with experiments over a wide range of pressure, temperature and equivalence ratios in most applications. Table 5.1 shows the full 21 reaction mechanism and the corresponding rate parameters.

An N species chemical reaction has the form

$$\sum_{k=1}^{N} \nu'_k S_k \rightleftharpoons \sum_{k=1}^{N} \nu''_k S_k, \tag{5.22}$$

where S_k stands for the kth species in a mixture, and ν'_k, ν''_k denote the molar stoichiometric coefficients of species k as reactant and product, respectively.

Table 5.1: Detailed chemical kinetic mechanism table. Reactions that include the symbol M involve third-body reactants. The third body is an inert molecule that is essential for a specific reaction to proceed. The reaction rates depend on the concentrations of third body with their specific efficiencies. A, n and E are related by $k = AT^n e^{-E/RT}$, units are mol/cm^3, s^{-1}, K and KJ/mol, respectively. $^a M = 2.50[H_2] + 12.00[H_2O] + 1.0[Other]$. $^b M = 2.00[H_2] + 6.0[H_2O] + 1.0[Other]$

Reaction		A	n	E
Hydrogen-oxygen chain				
$1. H + O_2 \rightarrow OH + O$		3.52×10^{16}	-0.7	71.4
$2. H_2 + O \rightarrow OH + H$		5.06×10^{4}	2.7	26.3
$3. H_2 + OH \rightarrow H_2O + H$		1.17×10^{9}	1.3	15.2
$4. H_2O + O \rightarrow OH + OH$		7.60×10^{0}	3.8	53.4
Direct recombination				
$5^a. H + H + M \rightarrow H_2 + M$		1.30×10^{18}	-1.0	0.0
$6^a. H + OH + M \rightarrow H_2O + M$		4×10^{22}	-2.0	0.0
$7^a. O + O + M \rightarrow O_2 + M$		6.17×10^{15}	-0.5	0.0
$8^a. H + O + M \rightarrow OH + M$		4.71×10^{18}	-1.0	0.0
$9^a. O + OH + M \rightarrow HO_2 + M$		8.00×10^{15}	0.0	0.0
Hydroperoxyl reactions				
$10^a. H + O_2 + M \rightarrow HO_2 + M$	k_0	5.75×10^{19}	-1.4	0.0
	k_∞	4.65×10^{12}	0.4	0.0
$11. HO_2 + H \rightarrow OH + OH$		7.08×10^{13}	0.0	1.2
$12. HO_2 + H \rightarrow H_2 + O_2$		1.66×10^{13}	0.0	3.4
$13. HO_2 + H \rightarrow H_2O + O$		3.10×10^{13}	0.0	7.2
$14. HO_2 + O \rightarrow OH + O_2$		2.00×10^{13}	0.0	0.0
$15. HO_2 + OH \rightarrow H_2O + O_2$		2.89×10^{13}	0.0	-2.1
Hydrogen peroxide reactions				
$16^b. OH + OH + M \rightarrow H_2O_2 + M$	k_0	2.30×10^{18}	-0.9	-7.1
	k_∞	7.40×10^{13}	-0.4	0.0
$17. HO_2 + HO_2 \rightarrow H_2O_2 + O_2$		3.02×10^{12}	0.0	5.8
$18. H_2O_2 + H \rightarrow HO_2 + H_2$		4.79×10^{13}	0.0	33.33
$19. H_2O_2 + H \rightarrow H_2O + OH$		1.00×10^{13}	0.0	15.0
$20. H_2O_2 + OH \rightarrow H_2O + HO_2$		7.08×10^{12}	0.0	6.0
$21. H_2O_2 + O \rightarrow HO_2 + OH$		9.63×10^{6}	2.0	2.0

5.2.1 General Reaction Rate Model

The reaction rate r_j depends on rate coefficients and species concentrations [29],

$$r_j = k_{fj}(T) \prod_{k=1}^{n} \left(\frac{\rho Y_k}{M_k} \right)^{\nu'_{kj}} - k_{bj}(T) \prod_{k=1}^{n} \left(\frac{\rho Y_k}{M_k} \right)^{\nu''_{kj}} \tag{5.23}$$

where k_{fj} and k_{bj} represent forward and backward rate coefficients, which are functions of the temperature T. Y_k and M_k are the mass fraction and the molecular weight of the species k, and ν'_{kj} and ν''_{kj} are reaction j's stoichiometric coefficients of species k on the reactant and product side.

The modeling of the rate coefficients k_{fj} and k_{bj} is an important issue for combustion processes. The Arrhenius law is widely used to calculate the forward rate coefficient

$$k_{fj} = A_j T^{n_j} \exp\left(\frac{-E_j}{RT} \right). \tag{5.24}$$

Here A_j is the pre-exponential constant, n_j the temperature exponent, and E_j the activation energy, all with respect to reaction j. These constant values are components of a complete description of the chemical scheme as provided by the scientific literature, and should be available as input for numerical computation, often in tabulation form. Backward rate coefficients k_{bj} are calculated from k_{fj} and the equilibrium constant for reaction j by

$$k_{bj} = \frac{k_{fj}}{\left(\frac{p_0}{RT}\right)^{\sum_{k=1}^{n} \nu_{kj}} \exp\left(\sum_{k=1}^{n} \nu_{kj} \left(\frac{\Delta S_{kj}}{R} - \frac{\Delta H_{kj}}{RT}\right)\right)}. \tag{5.25}$$

Here, $p_0 = 1.0133 \times 10^5$Pa, while ΔS_{kj} and ΔH_{kj} represent entropy and enthalpy changes for species j.

For reactions that involve a third body effect, the reaction rate also depends on the concentrations of third body components weighted by their efficiencies so that the reaction rate coefficient is multiplied by a factor c_M

$$c_M = \sum_{i=1}^{n} \eta_i c_i, \tag{5.26}$$

where η_i is the chaperon efficiency of species i.

For some reactions, a more accurate reaction rate formula is needed to account for the pressure and temperature dependencies. In this case, Troe's fitting formula [38] is a popular approach, and the forward rate coefficient is given by

$$k = F k_\infty k_L, \tag{5.27}$$

where the Lindermann-Hinshelwood form is

$$k_L = \frac{k_0[M]/k_\infty}{1 + k_0[M]/k_\infty}. \tag{5.28}$$

k_0 and k_∞ are still computed by the Arrhenius law, and the corresponding parameters A_0, A_∞, n_0, n_∞, E_0 and E_∞ are still provided by the mechanism

table. $[M] = p/RT$ is the molar density of the gas mixture. A broadening factor F to reduce the synthetic errors of the above form of k_L is given by

$$\begin{aligned} \log_{10}F &= \frac{\log_{10}F_c}{1+\left(\log_{10}[k_o[M]/k_\infty]\frac{1}{N}\right)^2}, & (5.29)\\ N &= 0.75 - 1.27\log_{10}F_c. & (5.30) \end{aligned}$$

The forms of the pressure dependent term F_c are usually empirical expressions, and can be fit as a function of temperature by

$$F_c = (1-\alpha)\exp(-T/T^{***}) + \alpha\exp(-T/T^{*}) + \exp(-T^{**}/T), \qquad (5.31)$$

in which α, T^*, T^{**} and T^{***} are adjustable parameters and should also be provided as part of a mechanisms table.

Given all the reactions in which a certain species k participates, either as reactant or as product, we can thus define the rate of production of species k and the heat release Hr_j of reaction j as

$$\dot{m}_k = M_k \sum_{j=1}^{n} \nu_{kj} r_j, \quad Hr_j = \sum_{k=1}^{N} h_k M_k \nu_{kj} r_j, \qquad (5.32)$$

where r_j is the reaction rate for reaction j, and h_k is the enthalpy of species k.

5.2.2 Reduced Chemical Mechanism

The chemistry calculation contributes substantially to the cost of the reactive flow simulations. Analysis shows that when chemistry source terms are calculated and provided as functions of species concentrations in a system of ordinary differential equations (as suggested by the finite rate chemistry approached discussed in the previous section), the convergence of the chemistry step is a major computation bottleneck. This is also the case for the three-dimensional Scramjet simulation discussed in Section 6. Decreasing both the number of species and the number of reactions has the advantage of significantly decreasing simulation complexity.

We consider a reduction of complexity from a global point of view. In the detailed mechanism stated above, there are eight reacting species involved: $H_2, O_2, H_2O, H, O, OH, HO_2$ and H_2O_2, and therefore eight corresponding differential equations. Among these species, H and O are not independent, they are simply rearranged among other species, thus leaving only six independent equations with nonzero chemical source terms. Therefore, algebraic relations among hydrogen-oxygen combustion system indicate that there exists at most six overall chemical steps.

The introduction of reduced mechanism is proposed when it is noted that many elementary reactions have very little contribution to the whole reaction process. There are a number of reduced mechanisms proposed in the combustion literature. By analyzing the role and importance of each of

Table 5.3: Four-step reduced mechanism

(I)	$H + O_2$	$\rightleftharpoons$	$OH + O$
(II)	$O + H_2 + M$	$\rightleftharpoons$	$H + OH + M$
(III)	$OH + H_2$	$\rightleftharpoons$	$H + H_2O$
(IV)	$H + H + M$	$\rightleftharpoons$	$H_2 + M$
	w_I	$=$	$w_1 + w_6 + w_{12} + w_{15} - w_{17}$ $+ w_{18} - w_{20} + w_{21}$
	w_{II}	$=$	$w_2 - w_3 + w_6 + w_{12} + w_{14}$ $+ w_{16} + w_{17} + w_{18} + w_{21}$
	w_{III}	$=$	$w_3 + w_4 + w_8 + w_{10}$ $+ w_{13} + w_{15} + w_{18}$
	w_{IV}	$=$	$w_5 + w_9 + w_{10} - w_{12}$ $+ w_{16} + w_{17} + w_{20}$

the elementary reactions of the detailed mechanism, and assuming further that two intermediate species H_2O_2 and HO_2 are both in steady state, a four-step mechanism has been found to provide an accurate flame structure for laminar diffusion flames [39]. The four elementary reactions chosen out of the 21 from the detailed mechanism, along with their algebraic combinations are given in Table 5.3.

The steady state assumptions are shown [39] to provide accurate combustion process, including ignition, extinction and heat-release phenomena for numerical calculations for hydrogen flames at atmospheric pressure and with low boundary temperatures. The coefficients are usually optimized or fit to give correct key species concentration, maximum temperature and laminar premixed flame speeds.

5.3 Flame Structures

5.3.1 Premixed Flame

In a premixed flame, the fuel and oxidizer are mixed perfectly before they are injected into the combustion chamber. Because of its more analytically explainable features, premixed flames can be regarded as a building block and a first step towards the study of more complicated flame structures. The mass stoichiometric ratio defined as [29]

$$\left(\frac{Y_O}{Y_F}\right)_{st} = \frac{\nu_O^{'} M_O}{\nu_F^{'} M_F} = s \tag{5.33}$$

and the equivalence ratio of the mixture

$$\phi = s\frac{Y_F}{Y_O} = \frac{\left(\frac{Y_F}{Y_O}\right)}{\left(\frac{Y_F}{Y_O}\right)_{st}} \tag{5.34}$$

are two central parameters commonly used to indicate the richness of combustion regimes, with $\phi > 1$ for rich combustion, when the fuel is in excess and $\phi < 1$ for lean combustion, when the oxidizer is in excess. Here, Y_F and Y_O stand for the mass fractions of fuel and oxidizer, respectively.

The determination of flame thickness is crucial to the numerical simulation of reacting flows. The flame structure should be resolved with enough cells located in the flame front. There are several ways to define the width of a flame δ_L^0. For numerical purposes, a practical formula is proposed from

the temperature profile [29]

$$\delta_L^0 = \frac{T_{\mathbf{max}} - T_{\mathbf{min}}}{\max\left(\left|\frac{\partial T}{\partial x}\right|\right)}. \tag{5.35}$$

5.3.2 Diffusion Flame

In a diffusion flame, the fuel and oxidizer are not premixed. They are added into a combustion chamber separately through different inlets. In distinction to a premixed flame, the mixing is characterized by a global equivalence ratio

$$\phi_g = s\frac{\dot{m_F}}{\dot{m_O}}, \tag{5.36}$$

where $\dot{m_F}$ and $\dot{m_O}$ are the flow rate of fuel and of oxidizer respectively.

Compared to a premixed flame, diffusion plays a much more important role here. The chemical reactions take place primarily near the area where fuel and oxidizer are not far from the stoichiometric ratio. Burning is far less efficient than for a premixed flame, considering the lack of either fuel or oxidizer on the far end of both sides. Furthermore, the flame speed and the thickness of the diffusion flame are not as well-defined as for premixed flames, the former due to the inability of the flame to propagate towards the fuel, and the latter due to the slow yet steady growth of the reaction zone as the time progresses. However, when a fixed time frame is considered (a flow through from the fuel inlet to the outlet of the Scramjet combustor for example), the range of the reaction zone can still be defined. In fact, the

full width at half maximum (FWHM) of the temperature profile is widely considered to be a characteristic flame thickness of diffusion flames. This definition is used in the present context to study the diffusion flame and its mesh requirements.

5.3.3 Thickened Flame Model

The thickened flame model is a method developed to thicken the flame front artificially, to allow numerical solution of the flame front on a coarse grid. The level of increased thickness is achieved by decreasing the pre-exponential constant A of the previously discussed Arrhenius form by a factor of TF, and increasing by the same factor the level of the species and heat diffusion coefficients. Theories of laminar flame structure show that the expression of flame speed and flame thickness scale like

$$s_L^0 \propto \sqrt{D_{th}^1 R_r}, \quad \delta_L^0 \propto \frac{D_t h}{s_L^0}, \tag{5.37}$$

where D_{th}^1 and R_r are the diffusion coefficient and mean reaction rate, respectively. Therefore, by replacing D_{th} by TFD_{th} and A by A/F, the reaction rate R_r is replaced by R_r/TF, the thickened flame propagates at the same laminar flame speed s_L, but with a flame width thickened to $TF\delta_L^0$. Choosing a sufficiently large TF (between 10 to 100 in most cases) allows the flame to be resolved on an LES grid [40].

It is shown in Section 5.5.3 that thickened flame model tends to produce

increased errors when modeling diffusion flames. In fact, the thickened flame model was originally derived for premixed flames. To adapt thickened flame to the case of diffusion flames and more complicated flame regimes, a new model to replace the constant thickening factor with a local variable that depends on space and time was proposed by J. P. Legier et.al in [40]. As the name suggests, the dynamically thickened flame (DTF) model adjusts the thickening factor dynamically across the whole region. The idea is to maintain the specified thickening level inside the combustion zone, while suppressing it away from the flame front. In this way, mixing is correctly represented outside the reaction zone and the flame itself still maintains enough thickness to be resolved.

In its original form, an indicator used to determine the range of combustion is defined by

$$\Omega = Y_F^{\nu_F} Y_O^{\nu_O} \exp\left(-\Gamma \frac{T_a}{T}\right), \tag{5.38}$$

where T_a is the activation temperature and Γ (> 1) is a specified parameter that further decreases the activation temperature. The sensor is then applied to obtain the variable thickening factor in

$$TF = 1 + (TF_{\max} - 1)\tanh\left(\beta \frac{\Omega}{\Omega_{\max}}\right). \tag{5.39}$$

Here, $\Omega_{\max}$ is the maximum possible value of Ω and β is another parameter that controls the thickness of the transition layer between thickened and non-thickened zones [40]. In the present analysis, we replace the indicator Ω with

the local reaction rate which serves the same purpose. Simulation results show that the major flame properties (flame thickness, mean concentration of OH and HO_2, ignition delay, etc.) stay at the same level as when applying the original thickened flame model using the same thickening values. This implies that DTF retains the effect of the TF model within the flame region, with the additional benefit that outside of the region, diffusion rates are not affected by the model. Moreover, the parameter β provides increased flexibility in adjusting the thickening at the edge of the flame front.

5.4 Combustion Models

5.4.1 The Flamelet Model

To derive the model, we begin with the continuity equation

$$\frac{\partial \rho}{\partial t} + \frac{\partial \rho u_i}{\partial x_i} = 0, \tag{5.40}$$

where ρ is the density, u_i is the i^{th} velocity component, and t is time. When dealing with a mixture of several species, a continuity equation is required for each of them. In the species equation, an extra term appears due to the rate of production of that species by chemical reactions. This quantity is denoted by $\dot{m}_i$. Therefore, the continuity equation for the partial density ρ_i of species i can be written as

$$\frac{\partial \rho Y_k}{\partial t} + \frac{\partial}{\partial x_i}\left(\rho(u_i + V_{k,i})Y_k\right) = \dot{m}_k, \tag{5.41}$$

where ρ_i and $V_{k,i}$ refer to partial density and diffusion velocity.

After applying Fick's law, the above can be rewritten as

$$\frac{\partial \rho Y_k}{\partial t} + \frac{\partial \rho Y_k u_i}{\partial x_i} - \frac{\partial}{\partial x_i}\left(\rho D \frac{\partial Y_k}{\partial x_i}\right) = \dot{m}_k. \tag{5.42}$$

The key idea of the flamelet approach is a change of variables within the diffusion flame sheets. The underlying assumption is that the structure of the flame depends on the mixture fraction Z and time t only, so that temperature and species mass fractions can be expressed as $T = T(Z,t)$ and $Y_k = Y_k(Z,t)$. Therefore, when a variable change is exercised on species equations from (x_1, x_2, x_3, t) to (Z, y_1, y_2, t), the gradient terms with respect to the directions of y_1 and y_2 can be neglected when comparing to the terms normal to the flame. Here y_1 and y_2 are spatial variables orthogonal to each other in the plane normal to direction defined by Z. The assumption implies that x is represented uniquely by the mixture fraction coordinate Z, and that the reaction zone is smaller than the small scales of the turbulence. The flamelet derivation is restricted to a small region of locally laminar flow around the reaction zone.

After converting to local coordinates (Z,t) and rearranging terms

$$\begin{aligned} \rho\frac{\partial Y_k}{\partial t} + Y_k\left(\frac{\partial \rho}{\partial t} + \frac{\partial}{\partial x_i}(\rho u_i)\right) \quad &+ \quad \frac{\partial Y_k}{\partial Z}\left(\rho\frac{\partial Z}{\partial t} + \rho u_i \frac{\partial Z}{\partial x_i} - \frac{\partial}{\partial x_i}\left(\rho D \frac{\partial z}{\partial x_i}\right)\right) \\ &- \quad \rho D\left(\frac{\partial Z}{\partial x_i}\frac{\partial Z}{\partial x_i}\right)\frac{\partial^2 Y_k}{\partial x^2} = \dot{m}_k. \end{aligned} \tag{5.43}$$

The factors within the parentheses of the second and third terms on the left of Equation 5.43 vanish due to conservation of mass and species equation, and the equation becomes

$$\begin{aligned} \rho\frac{\partial Y_k}{\partial t} &= \dot{m}_k + \rho D\left(\frac{\partial Z}{\partial x_i}\frac{\partial Z}{\partial x_i}\right)\frac{\partial^2 Y_k}{\partial Z^2} \\ &= \frac{1}{2}\rho\chi\frac{\partial^2 Y_k}{\partial Z^2} + \dot{m}. \end{aligned} \tag{5.44}$$

In this way, the flamelet model effectively reduces the system of species equations to one dimension, the so-called Z-space. The variable $\chi = 2D\left(\frac{\partial Z}{\partial x_i}\frac{\partial Z}{\partial x_i}\right)$ is called the scalar dissipation rate. It is a key variable in the flamelet equation; it controls mixing and measures molecular fluxes between different species in directions normal to the flame front. Once χ is specified, the combustion problem is solved and the flame structure provided. In other words, the hydrodynamics has been removed from the chemistry in Equation 5.44, which is a pure reaction diffusion equation. The steady flamelet model assumes further that the flame structure is in steady state, and the flamelet equation can be simplified to

$$\frac{1}{2}\rho\chi\frac{\partial^2 Y_k}{\partial Z^2} + \dot{m} = 0. \tag{5.45}$$

One approach to simulating the Scramjet flow structure is to use the flamelet model described above. The model is computationally efficient in that the flamelet solutions can be precomputed and tabulated for further use,

given specific boundary conditions. These tables describe scalar variables as functions of Z and χ. When the flow equations are solved in main simulation, a table lookup is then conducted for each cell.

5.4.2 Finite Rate Chemistry

As Section 5.4.1 suggests, one significant assumption inherent in the flamelet model is that the flame is considered to be a locally one-dimensional structure, and quantities that account for gradients parallel to the flame front are therefore ignored. A numerical scheme based on this assumption may not accurately model flame configurations in many practical problems, especially when turbulence plays a major role in the flame development.

Finite rate chemistry is a method developed here to characterize turbulent combustion processes as an alternative to the flamelet model. It is based on the notion that turbulence occurs on many different levels of length scales, and that the chemistry time and length scales lie somewhere between the smallest turbulence length scale (the Kolmogorov scale) and the larger end of it. Therefore, it is possible that combustion process can be resolved on a larger scale than the levels needed to resolve turbulence. As an advantage, the model does not rely on the laminar flame structure assumption. Instead, the combustion processes and rate of chemical reactions are calculated directly with data provided by chemical-kinetic mechanisms. A system of ordinary differential equations as shown in (5.46) based on the reacting species are then solved at each time step to account for the change in species concentration

due to the combustion process.

$$\frac{\mathrm{d}Y_k}{\mathrm{d}t} = \dot{m}_k = M_k \sum_{j=1}^{n} \nu_{kj} r_j. \quad (k = 1, ..., N) \tag{5.46}$$

5.5 Finite Rate Chemistry Modeling in One Dimension

In this section, the finite rate chemistry model discussed in Section 5.4.2 is investigated in a one-dimensional framework. The reduction of chemical-kinetic mechanism and thickening factors are both related to the quality of simulation results. The purpose of the investigation is to analyze the accuracy of these approaches and to provide necessary guidance to the mesh resolution needed to perform a full-domain numerical simulation of a three-dimensional Scramjet turbulent combustion problem.

5.5.1 Simulation Setup

To simulate one-dimensional combustion, various formulations can be developed to study different types of flames [29, 41, 42]. In this context, initial conditions are set up consistent with the three-dimensional Scramjet flow configurations. Densities, temperatures, velocities and species partial densi-

ties are set to be

$$x = 0: \qquad \rho_L = \rho_{H_2} = 1.241 \times 10^{-4},\ T_L = 300K,\ v_L = 0, \tag{5.47}$$

$$x = L: \qquad \rho_R = \rho_{O_2} = 1.241 \times 10^{-4},\ T_R = 1500K,\ v_R = 0. \tag{5.48}$$

The partial densities are the configuration of a diffusion flame. To study a premixed type of flame, a stoichiometric mixture of hydrogen and oxygen is considered, so that $\rho_{H_2} = \frac{1}{1+s}\rho$ and $\rho_{O_2} = \frac{s}{1+s}\rho$ on both ends.

A solution for this boundary value problem can be found by discretizing the spatial domain with appropriate numerical schemes. The WENO scheme as described in Section 4.2 combined with finite rate chemistry discussed in Section 5.4.2 are applied here to study the flame structure, which is a simplified version of the combustion process taking place inside the Scramjet combustor. Both the detailed chemical-kinetic mechanism in Table 5.1 and the reduced version in Table 5.3 are employed. In addition, it is assumed that all binary diffusion coefficients are constant and equal: $D = D_k = 10^{-3}$. Viscosity and thermal conductivity are determined according to Section 5.1.

The simulation consists of five parts: the chemistry data input (chemistry-kinetic mechanism table and thermodynamic table), the reaction table parser and species and reaction data structures, the general numerical scheme, the equation of state library, and the finite rate chemistry ordinary differential equation solver.

5.5.2 The One Dimensional Flame Structure

A typical simulation result of the one-dimensional flame structures for premixed and diffusion flames is illustrated in Figure 5.1.

The structure of a premixed flame can be roughly divided into four parts: the unburned mixture, the preheat zone, the reaction zone and the burned mixture. In unburned and burned zones, temperature and concentration of fuel/oxidizer are almost constant. In the preheat zone, temperature starts to grow due to the amount of net heat release contributed by exothermic reactions. It is the region where the unburned gas mixture is heated up by conduction. The reaction zone follows the preheat zone, and is the region where major reactions take place. The gas mixture coming out of the reaction zone then enters the burned gas zone where temperature reaches a high level and stays constant again. Also shown in Figure 5.1 are the mass concentration profiles of the fuel H_2, the oxidizer O_2, and OH, a product species of major importance in hydrogen-oxygen combustion.

The grid resolution needed to resolve a hydrogen-oxygen premixed flame is generally considered impractical for most simulation purposes, with a flame width roughly in the order of between 10^{-2} cm to 10^{-1} cm [16,43,44], meaning that the mesh size for a well-resolved combustion scheme should be at least in the order of 10^{-3} cm (to guarantee about 10 cells inside of the flame front). This range of flame widths is verified by the one-dimensional simulations performed here at a mesh size of 0.001 cm to about 0.05 cm, using the flame

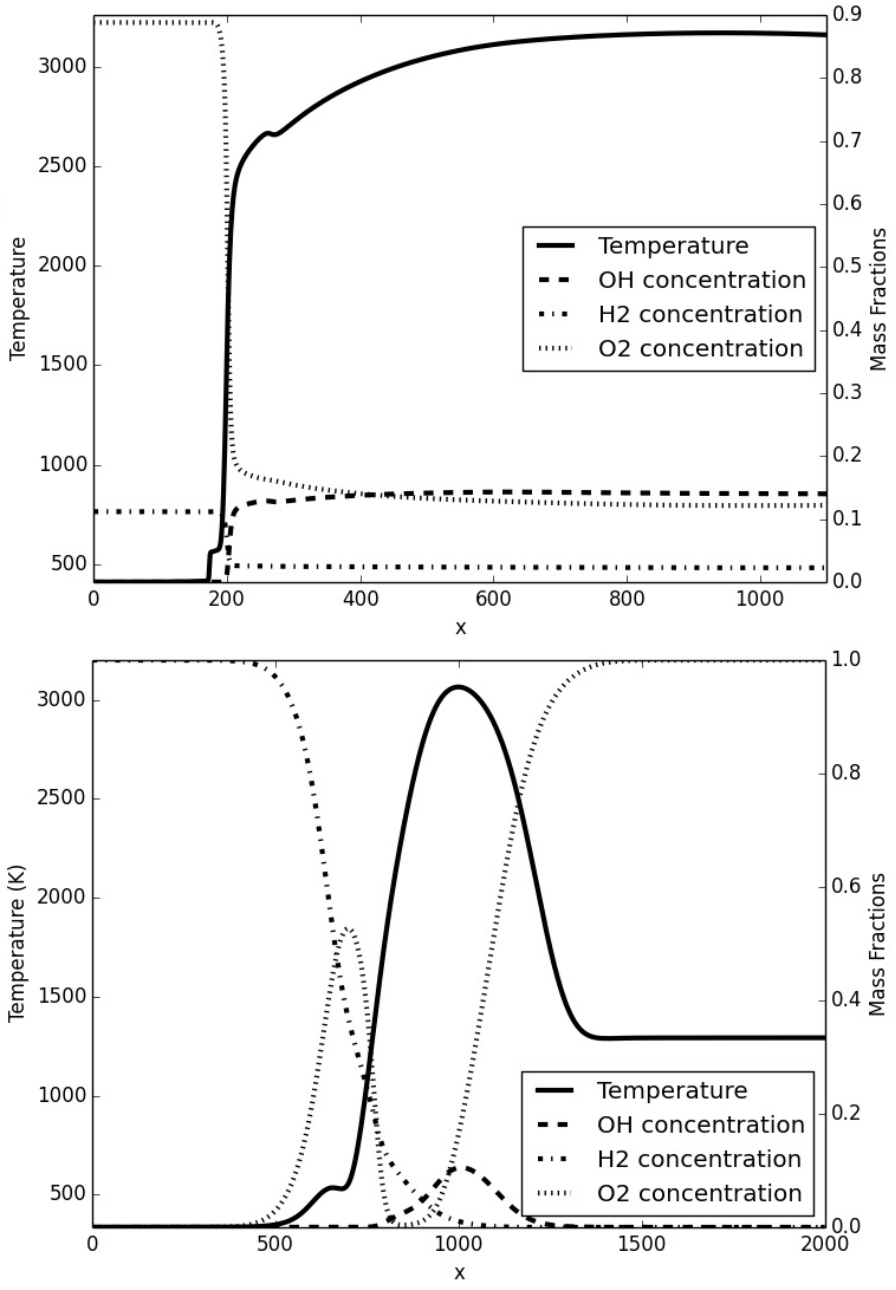

Figure 5.1: The flame structure of premixed (upper) and diffusion (lower) flames. The variables included are temperature and the mass fractions of the oxidizer (O_2), the fuel (H_2) and one indicator product species OH.

width formula given by Equation 5.35.

As Figure 5.1 shows, a diffusion flame exhibits a very different flame structure. The combustion is dominated by the rate of mass diffusion between the fuel (H_2) and the oxidizer (O_2). Generally speaking, the burning is far less efficient, as the close to unity mass fractions of fuel and oxidizer away from the flame zone indicate. On the other hand, it can be seen that the mass concentration of species OH is a good indicator of the temperature level in both premixed and diffusion flames.

Due to the effect of mass diffusion, the width of a diffusion flame is generally much thicker than that of a premixed flame. For this reason, modeling a diffusion flame is less restrictive in terms of grid resolution requirement. However, when the thickened flame model is applied to a flame with a more complex regime, as is the case of a flame inside a combustion chamber, the flame profile and the combustion process may be more susceptible to a change caused by the thickening factor, and therefore the flame structure may not be correctly predicted.

The effectiveness of the thickened flame model and its influence on the key properties of the flame structure are discussed below.

5.5.3 Thickened Flame and Grid Resolution

In this section, we investigate the effect of the thickened flame model and the level of reduction in chemical mechanism on the quality of the one-dimensional flame structure by performing a list of tests that are aimed at

capturing the major flame characteristics. A combination of model parameters that give the correct flame predictions are to be derived.

As discussed in Section 5.5.2, premixed flames are generally hard to resolve. The thickened flame model can therefore be employed to reduce the mesh requirements needed to resolve a premixed flame. A flame is generally considered to be resolved if certain indicator parameters of the flame are preserved and shown to be insensitive to changes in discretization size (and thus are converging to the true value). In this section, three such indicator parameters are investigated, namely, the laminar flame speed, the peak mass fraction of OH (a major product of general interest) and the peak mass fraction of HO_2 (a very active intermediate radical species). The last quantity is generally considered to be difficult to achieve convergence for because of its unstable nature and due to the fact that it is produced in considerable amount only in a very thin layer of reaction zone, which is coincident with the location of the flame front.

On the other hand, a diffusion flame maintains a very different structure, and the flame speed is not well-defined. In addition to this, species mass productions are not conserved quantities across different levels of mesh size. Due to the extent of mass diffusion, finer grids generally contribute to more burning, and therefore higher proportions of product species. What turns out to be an important indicator for a diffusion flame is the delay in ignition time. The ignition time of a flame regime can be roughly divided into the time delay due to mixing and the delay for the activation energy to be reached

and the chemical reactions to occur. While the first type of delay is almost negligible for a premixed flame, it could be quite significant for a diffusion flame. Moreover, the combined effects of thickened flame model (increases diffusion while decreasing reaction rates) tend to further delay the ignition, and the amount of heat release produced by combustion. Therefore, the ignition time is instead studied as a criteria in the case of diffusion flames.

5.5.3.1 Premixed Flame The laminar flame speed is computed using a number of grid sizes ranging from $\Delta x = 0.001\,\text{cm}$ to $\Delta x = 0.09\,\text{cm}$. The thickened flame model is applied on three levels: $TF = 1$ (i.e. no thickening), $TF = 5$ and $TF = 10$. Both full and reduced chemical mechanisms are considered. The objective is to find the coarsest mesh size in each combination of TF and chemistry model that predicts the flame speed to an acceptable degree. The flame speed and species mass fractions calculated under the finest mesh size $\Delta x = 0.001\,\text{cm}$ are considered as benchmark values. When different levels of thickening factor are imposed, the flame speed at this finest grid stays at around 76 cm/ms, the mass fraction $Y_{HO_2} \approx 0.325\%$ and $Y_{OH} \approx 14.46\%$, for both full and reduced mechanisms. The thickness of flame is evaluated to be about 0.04 cm, a level clearly not resolvable under the current Scramjet mesh size of 0.05 cm. Using a maximum allowed 10% error in the flame speed and the mass fraction of species as the acceptance level, results are shown in Figure 5.2.

The result indicates a few points.

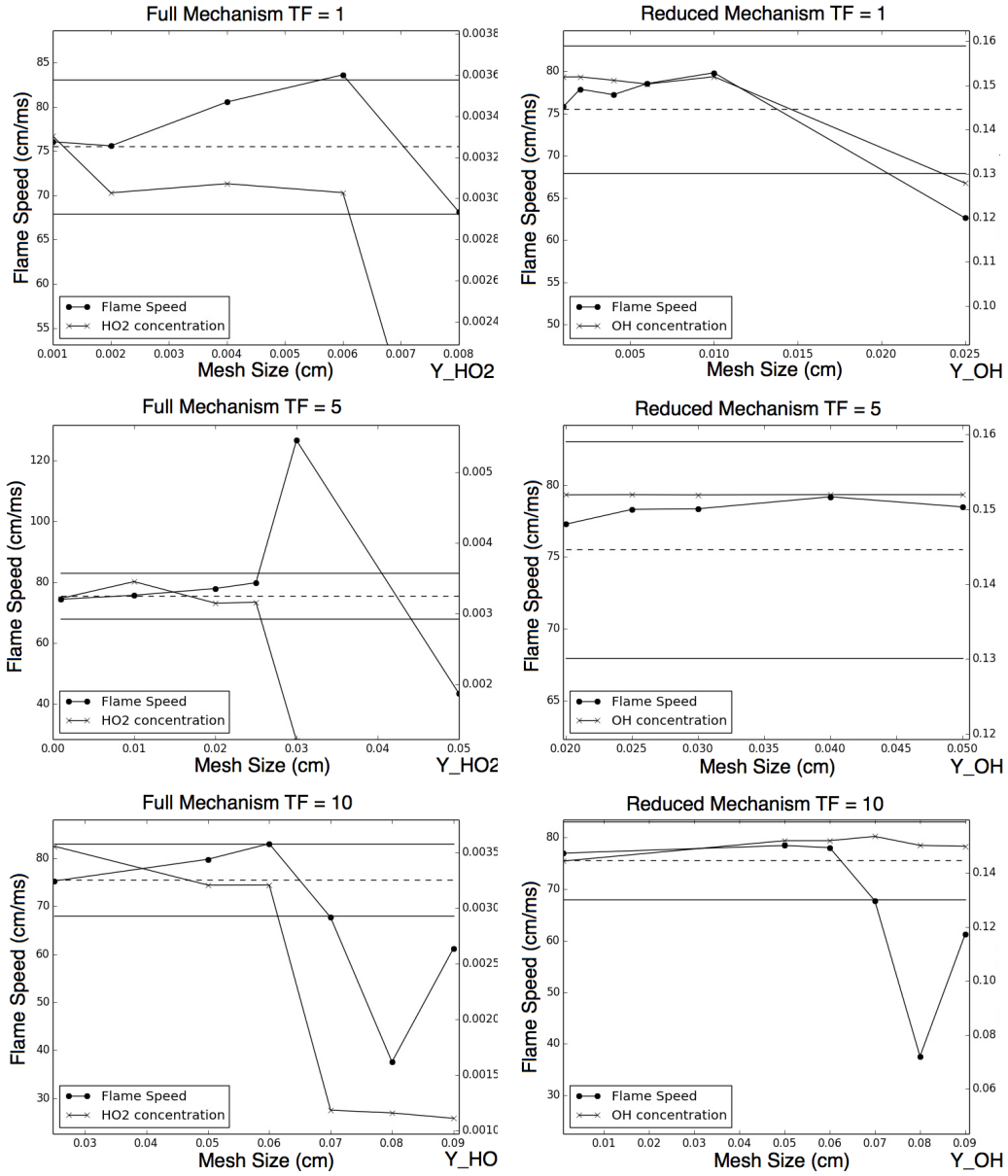

Figure 5.2: Simulated premixed flame speed and species concentration (HO_2 for full chemistry and OH for reduced chemistry) against a selection of mesh sizes. Full chemistry (left column) and reduced chemistry (right column) with no thickening $TF = 1$ (row 1), $TF = 5$ (row 2), and $TF = 10$ (row 3). On these figures, the dotted horizontal lines indicate the correct chemistry while the solid horizontal line indicates the acceptance level.

1. When thickened flame is not applied ($TF = 1$), modeling combustion accurately requires a very high level of mesh refinement, in the order of 10^{-3} cm for full mechanism and around 10^{-2} cm in the case of reduced mechanism;

2. The thickened flame model effectively expands the width of the flame front, making it possible to resolve the flame width on a much coarser grid. Moreover, at least for small thickening ranges, the allowed coarsest mesh size is roughly proportional to the level of thickening;

3. A reduced chemical mechanism allows a much coarser grid size when it comes to modeling the flame speed. The reason is that reduced mechanisms are generally fit to the detailed mechanism in terms of the laminar flame speed. Fewer reactions with comparable reaction rates and the absence of unstable intermediate species also contribute to a more stable flame speed in contrast to the detailed mechanism;

4. The intermediate species HO_2 is assumed to be in a steady state when applying the reduced mechanism. Therefore in this case, OH is used as a replacement in the reduced mechanism plots. It becomes obvious from the plots that OH is a more stable product species comparing to HO_2, and it may be less indicative of the correct level of mesh size that can be used.

The mesh requirement results are summarized in Table 5.4.

Table 5.4: Premixed flame mesh requirements with respect to full and reduced chemistry mechanism and thickening factors $TF = 1$, $TF = 5$ and $TF = 10$. The mesh resolutions are based on a requirement for a maximum 10% error in flame speed and species mass fractions.

Full mechanism			Reduced mechanism		
$TF = 1$	$TF = 5$	$TF = 10$	$TF = 1$	$TF = 5$	$TF = 10$
0.004 cm	0.025 cm	0.05 cm	0.01 cm	> 0.05 cm	0.07 cm

One disadvantage of the thickened flame model is that the artificial thickening may alter other flame properties. Due to thickening, the interaction between the flame and the turbulent flow structure may be affected, especially flow structure on small scales. To reduce this effect, only the smallest possible thickening level should be used. The choice of thickening level is therefore not arbitrary. It is suggested in numerous literature (for example in [40]) that a thickening factor can take on values as large as 100, however, the study below shows that such extremes are both undesirable (for instance, causing the delay in ignition time as described in Section 5.5.3.2) and unnecessary for the present problem. Actually a limited thickening is sufficient to resolve the flame front at least in the flame configuration studied here.

The desired value of thickening factor to be applied has been considered by others. For instance, [45] proposes that a suitable value $TF_{\max}$ could be

$$TF_{\max} = \max\left(\frac{n\Delta_{mesh}}{\delta_l^0}, 1\right), \tag{5.49}$$

where Δ_{mesh} is the computational mesh size, δ_l^0 is the flame width, and n represents the number of cells inside of the flame front to resolve the thickness.

n is usually chosen in a empirical way, and 5 is considered an appropriate value. Instead, here we choose to determine the thickening level following the principle that the artificially thickened flames should still be able to maintain the macro flame structure and combustion properties. Figure 5.3 again gives the simulated results of the flame speed and species concentration of HO_2 for full chemical mechanism and OH for reduced chemical mechanism. A range of thickening factors from $TF = 1$ to $TF = 20$ are applied to determine the smallest acceptable value of TF, given a range of mesh sizes between 0.01 cm and 0.05 cm. Figure 5.3 shows the cases for $\Delta x = 0.05$ cm, which is consistent with the current Scramjet mesh resolution, and $\Delta x = 0.025$ cm, which is a further refined mesh size that can be used.

The result indicates that the coarser grid generally requires more thickening, as expected. The number of cells in the flame front determined in this way are 6 for the grid level of $\Delta x = 0.05$ cm and 8 for $\Delta x = 0.025$ cm, more demanding than given in (5.49). Also, the two parameters considered both tend to be less sensitive to an increase in thickening level. This does not mean that the flow features are correctly captured. To maintain a flame structure as close to the real flame as possible, only the smallest TF value should be applied. In addition, the plots on the reduced mechanism side indicate a constant over prediction of the species concentration of OH. This is an error inherent in the development of reduced mechanism, a topic to be discussed further in Section 5.5.3.3.

To summarize, a premixed flame needs to be thickened in most applica-

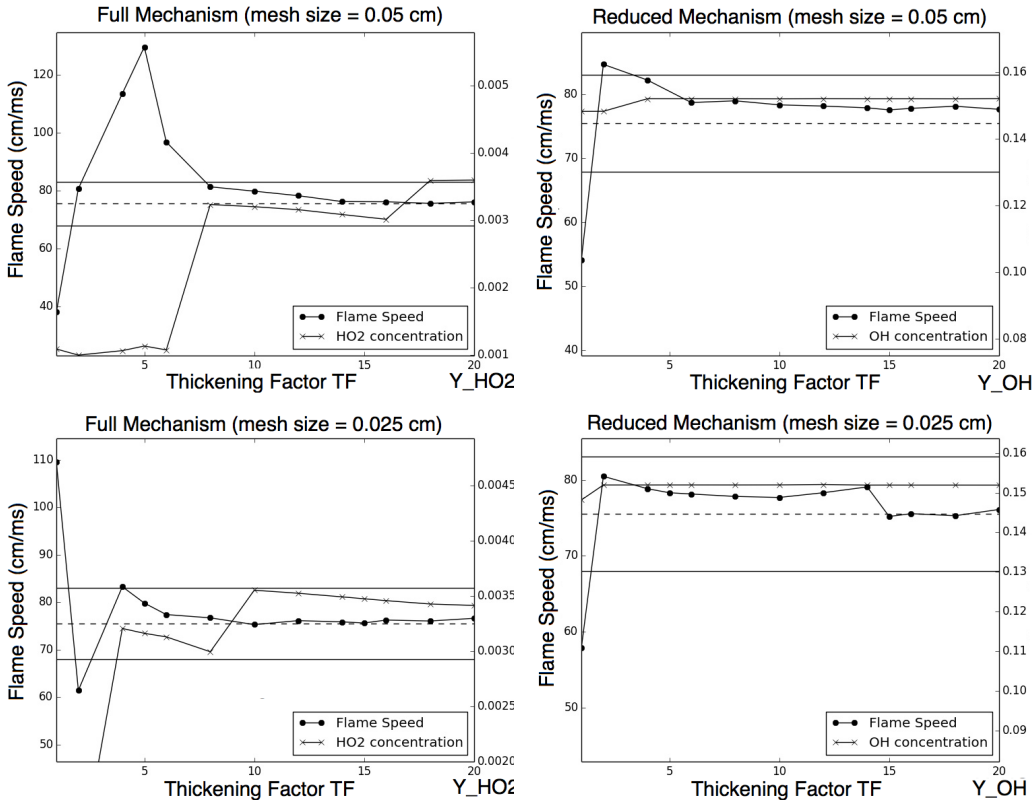

Figure 5.3: Simulated premixed flame speed and species concentration (HO_2 for full chemistry and OH for reduced chemistry) against a selection of thickening factors. Full chemistry (left column) and reduced chemistry (right column) with $\Delta x = 0.05\,\text{cm}$ (row 1) and $\Delta x = 0.025\,\text{cm}$ (row 2) are displayed. The meanings of dotted and solid horizontal lines have the same meaning as is described in Figure 5.2.

Table 5.5: The minimum level of thickening factor needed to resolve a premixed flame for grid resolution ranging from $\Delta x = 0.01\,\text{cm}$ to $\Delta x = 0.05\,\text{cm}$. Both the full and the reduced chemical mechanisms are considered.

Full chemical mechanism					
$0.01\,\text{cm}$	$0.02\,\text{cm}$	$0.025\,\text{cm}$	$0.03\,\text{cm}$	$0.04\,\text{cm}$	$0.05\,\text{cm}$
$TF_{\text{min}} = 2$	$TF_{\text{min}} = 3$	$TF_{\text{min}} = 5$	$TF_{\text{min}} = 6$	$TF_{\text{min}} = 6$	$TF_{\text{min}} = 8$
Reduced chemical mechanism					
$0.01\,\text{cm}$	$0.02\,\text{cm}$	$0.025\,\text{cm}$	$0.03\,\text{cm}$	$0.04\,\text{cm}$	$0.05\,\text{cm}$
$TF_{\text{min}} = 1$	$TF_{\text{min}} = 1$	$TF_{\text{min}} = 2$	$TF_{\text{min}} = 2$	$TF_{\text{min}} = 2$	$TF_{\text{min}} = 4$

tions, when mesh requirements are not met. On the other hand, thickening should not be introduced for more than needed. The minimum level of thickening factor for both full and reduced chemical mechanisms are studied, and the concluding results for premixed flames are summarized in Table 5.5.

5.5.3.2 Diffusion Flame Based on the results obtained by Section 5.5.3.1, this section goes on to examine the mesh requirements for correctly simulating a one-dimensional diffusion flame. As explained in Section 5.3.2, the thickness of a diffusion flame is defined in a different way. Because of its slowly developing nature, a steady flame front in the normal sense does not exist, unless the flame itself is stretched and certain conditions met [29]. In this context, we restrict the combustion time period to $T = 0.12\,\text{ms}$, which is approximately the time needed for the flow of fuel (H_2) to travel from the jet nozzle to the end of the Scramjet combustion chamber, and therefore the maximum time allowed for a diffusion type of flame to develop inside the chamber. The thickened flame model is applied in conjunction with both the

full and reduced chemical mechanisms. The flame width defined by FWHM described in Section 5.3.2 turns out to be much thicker than that of premixed flame under the same level of mesh resolution. The finest mesh in this study ($\Delta x = 0.001\,\text{cm}$) evaluates the diffusion flame thickness to be about $0.2\,\text{cm}$ at the end of the time period.

It is suggested in Section 5.3.2 that a diffusion flame is usually located where the mixture of fuel and oxidizer is close to a stoichiometric ratio, and the extent of mixing is an important factor in determining the efficiency of diffusion flame combustion. Therefore, artificial thickening may affect the diffusion flame structure more negatively comparing to a premixed flame, in view of the fact that the interactions between mass diffusion and chemical reactions are highly nonlinear. One of the major significant influences is on the ignition time of the combustion process. A delay of ignition to a certain degree could affect the flame profile as a whole and the extent of combustion, especially when the time period for combustion to take place and for the flame to develop is limited, as is the case here.

In the thickening analysis of the premixed flames, we restrict the range of TF that could be applied to a series of mesh sizes ranging from $\Delta x = 0.01\,\text{cm}$ to $\Delta x = 0.05\,\text{cm}$ in order to obtain simulation results within an acceptance level of 10%. Based on the result of minimum TF values in each cases as summarized in Table 5.5, we further determine in each case whether the minimum level of TF, when imposed on a diffusion flame, causes too much ignition delay.

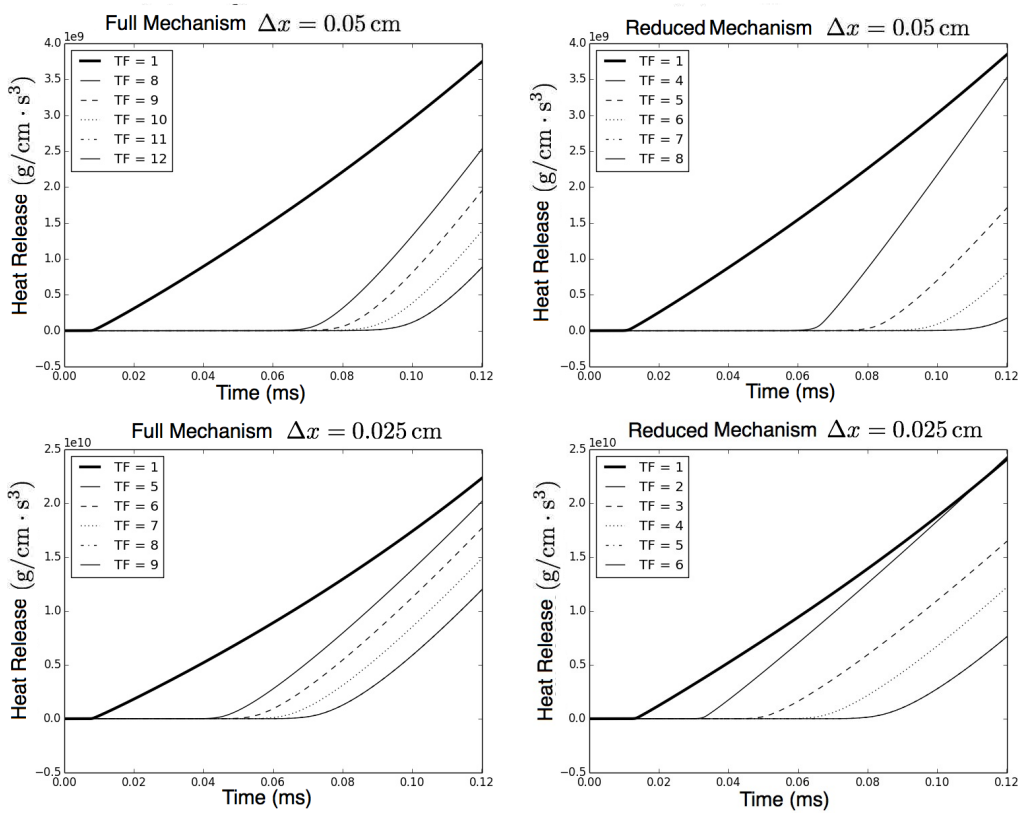

Figure 5.4: The evolution of diffusion flame heat release over the time period $T = 0.12\,\mathrm{ms}$. Thickening factors derived from the premixed flame analysis are applied in each case (left column for full mechanism, and right column for reduced mechanism).

Figure 5.4 illustrates the evolution of generated heat release over the time period $T = 0.12\,\mathrm{ms}$, for two levels of grid size $\Delta x = 0.05\,\mathrm{cm}$ to $\Delta x = 0.025\,\mathrm{cm}$ and two levels of chemical mechanism.

It can be seen from the figure that applying the thickened flame model generally postpone the flame ignition time. Between the two grid levels investigated here, the coarse grid ($\Delta x = 0.05\,\mathrm{cm}$) shows a larger discrepancy

between no thickening ($TF = 1$) and TF starts at 8 (the minimum value determined by premixed flame). The ignition is not started until a little more than half of allowed burning time has passed. Due to the delay, the total heat release at the end of simulation time is reduced by about 28%. With the reduced mechanism, where TF is justified to start from a smaller value, the delay is about the same extent, though after the point of ignition is passed, the rate of heat release increases rapidly, with an end heat release error stopping at around 8%.

With one more level of mesh refinement, the difference introduced by thickening factor narrows by a lot, partly due to the observation that a smaller TF could be applied with more mesh refinement. Considering the minimum TF levels for instance, the ignition delay amounts to 29% and 15%, the reduction in total heat release amounts to 9.6% and -0.01% for the full and reduced chemical mechanisms, respectively.

The dynamically thickened flame model introduced in Section 5.3.3 shows no large effect on flame features in the one-dimensional diffusion flame configurations. An analysis of the result shows that there is very little chemical reaction taking place outside of the reaction zone even without applying the dynamic model. This indicates that increased diffusion by thickened flame model has very little effect on the combustion profiles there. However, combustion processes in the three-dimensional framework is more complicated, with much more interaction between different types of flame structures. The dynamically thickened flame model could be more preferable due to its ability

to maintain the correct mixing profile.

The production of OH and HO_2 species discussed earlier turns out to be more sensitive to a change in thickening factor in a diffusion flame than in a premixed flame, a result of the strong correlation between thickening and diffusion as expected. Both species show an increase in total production rate due to increased diffusion, but still not comparable to the rate of production on a much refined grid. Generally speaking, the thickened flame model is favorable to combustion. Although applying the model tends to postpone the ignition time, it allows for more diffusion, thus more combustion without the needs to resort to a more refined grid for flame resolution.

As the discussion implies, the standard used in this context to determine the accuracy of thickened flame and reduced mechanism model are different for premixed and diffusion flames in certain respects. The two types of flames have very different structures and combustion dynamics. Reactions inside a premixed flame regime turn out to be more volatile, mainly attributed to the interactions (through mass diffusion and heat transfer) between the reaction zone and the zone with burnt gas (discussed in Section 5.5.2). The flame speed is generally considered to be a more suitable parameter for characterizing the dynamics of a premixed flame. In the case of a diffusion flame, on the other hand, the case is reversed. While the flame speed is not well-defined, the heat release is a quantifiable parameter because of the restricted region the combustion could take place. Detailed analysis shows that the reaction rates and heat release are both negligible outside of the diffusion

Table 5.6: The level of ignition delay (as the percentage of the total time) for the combinations of parameters that have passed the premixed flame resolution tests.

Full chemical mechanism						
Δx	0.01 cm	0.02 cm	0.025 cm	0.03 cm	0.04 cm	0.05 cm
$TF_{\min}$	2	3	5	6	6	8
Ignition delay	7%	15%	29%	36%	36%	50%
Reduced chemical mechanism						
Δx	0.01 cm	0.02 cm	0.025 cm	0.03 cm	0.04 cm	0.05 cm
$TF_{\min}$	1	1	2	2	2	4
Ignition delay	0	0	15%	16%	16%	43%

flame reaction zone (the length of which is defined as the flame width).

In summary, while it is shown in the case of a premixed flame that a too small thickening factor may fail to resolve the flame, our studies further indicates that for large TF, the structure of the flame and the combustion can also be effected by delayed burning. Combining the cases investigated above, a grid size of $\Delta x = 0.05\,\text{cm}$ should still be considered as too coarse for resolving a flame that combines both premixed and non-premixed flame structures. Using a $TF = 8$ would underpredict the level of combustion, a case to be further reviewed in Section 6. With one more level of mesh refinement, a grid size of $\Delta x = 0.02\,\text{cm}$ is suggested to give a more or less satisfactory prediction of the flame structure and burning as a whole, with no thickening ($TF = 1$) for a reduced chemistry mechanism. Table 5.6 further shows the ignition delay for the whole range of grid sizes investigated in the premixed flame section.

5.5.3.3 The Effect of the Reduced Chemical Mechanism in One-dimensional Framework

A detailed analysis of the rate of each reaction in the full chemical mechanism shows that each of these reactions reaches their maximum value around the ignition time, where the temperature (or heat release) profile achieves largest gradient. Among them, the hydrogen-oxygen chain reactions #3, #2 and #1 in the full mechanism Table 5.1 are the ones with the highest rates. After ignition time is reached, the dominant reactions in terms of reaction rates are #0, #1, #2, and #3, while all other reactions have rates much smaller, in the range of one to three magnitude of order. In terms of heat release, the combination step reaction #6 contributes the largest amount of thermal energy in forming the major product species H_2O.

The large difference in the range of reaction rates justifies a reduction of the detailed mechanism. As discussed in Section 5.2.2, globally reduced mechanisms have at most six steps in total in the case of hydrogen-oxygen flames. Various types and different levels of reduced chemical mechanisms can be found in literature, for example in [37, 39, 46–48]. These developed mechanisms are generally fit to be in agreement with either experimental data or simulation results with detailed mechanism for very different flame structures and combustion processes ranging from fuel-lean to fuel-rich configurations, low to high temperatures, deflagration, detonation or flame extinction processes, normal (1 atm) to high (over 10 atm) pressure, and so on. In this study, a few of the four-step reduced chemical mechanisms are tested, and the one found to be most consistent with the configuration studied here

is the one given in the reduced mechanism Table 5.3.

The investigated four-step reduced mechanism consists of three hydrogen-oxygen chain reaction steps (#1, #2, #3 in the detailed mechanism table) and one recombination step (#5 in the table). After a linear combination of the elementary intermediate steps, the rates of the resulting reactions are comparable and have about the same order of magnitude, among which reaction #4 in reduced mechanism produces the largest amount of heat. The previous discussion of a premixed flame in Section 5.3.1 shows that the reduced mechanism generally provides satisfactory agreement in terms of predicting flame speed and major characteristics of the flame. However, as Figure 5.4 suggests, ignition time inconsistency can still be seen with the reduced mechanism, when the same level of thickening is compared. The general approach of establishing a reduced mechanism is associated with leaving out reactions that have minor contributions to the whole scheme, or combining fast reactions into major reaction steps. During the reduction process, the accuracy in heat release and related effects are therefore reduced as well.

The major advantage of various reduced mechanisms is their efficiency in computational cost. Indeed, no matter what model is chosen, flamelet or finite rate chemistry, the combustion process modeling is alway an expensive procedure. With the flame configuration discussed in this section, a more than 10% reduction in running one flow through in Scramjet time scale is observed.

5.5.3.4 Conclusion This section discusses the finite rate chemistry approach being applied to the Scramjet configuration that is reduced to the one-dimensional case. The approach is evaluated together with the use of the thickened flame model that artificially expands the flame front, and with a reduced chemical mechanism that also reduces the time complexity of the whole simulation. It is shown here that the thickened flame model effectively increases the flame width while retaining the major flame features with enough accuracy. This allows for the flame to be resolved on a relatively coarse grid size. In another direction, the feasibility of a specific four-step reduced chemical mechanism is investigated. The result indicates that the reduced chemical mechanism generally agrees quite well with detailed mechanism, with slight delay in predicted ignition time. However, a combination of the mechanism with thickened flame model generally deteriorates the simulation results. The level of allowed thickening in order to retain the same amount of accuracy will be further restricted. In this case, more levels of mesh refinement will be needed in order to resolve the flame. To summarize, with a 10% acceptance level, the maximum mesh size allowed to resolve a flame in a one-dimensional framework is 0.01 cm for a full chemical mechanism, with a thickening factor $TF = 2$, and 0.02 cm for a reduced chemical mechanism, with no thickening ($TF = 1$).

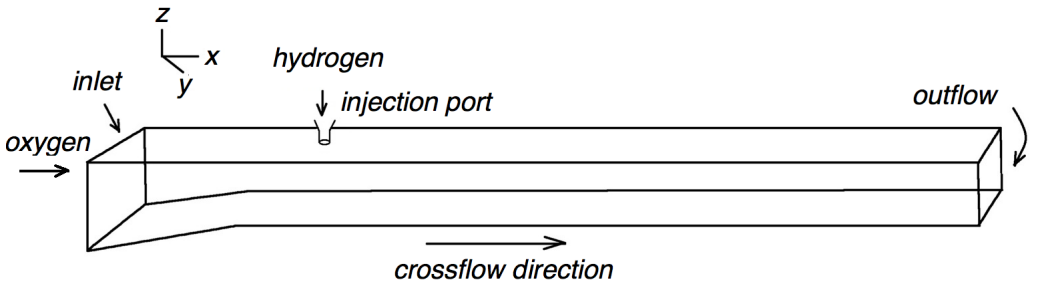

Figure 6.1: Sketch of a scramjet combustion chamber

6 Scramjet Modeling

6.1 Problem Configurations

The Scramjet studied in this work is an experimental Mach 7 aircraft. Combustion occurs within a combustion chamber with the flow still supersonic, but at a reduced Mach number $M = 2.4$. A model scramjet combustor has been developed, and experiments conducted in a Stanford 6" Expansion Tube Facility. The flow parameters are chosen to be representative of the flow conditions found in a combustion chamber. The details of the experiment setup can be found in [12]. Results from experiments and numerical simulations conducted at Stanford University Predictive Science Academic Alliance Program (PSAAP) are compared with simulation results presented in this section [49].

A sketch of a simplified Scramjet combustion chamber is shown in Figure 6.1. The dimensions of the model combustion chamber is $31\,\text{cm} \times 7.5\,\text{cm} \times 2.5\,\text{cm}$. There is an injection port with a diameter of $0.2\,\text{cm}$ located at the

center line of the top wall, with a distance to the flat plate leading edge $L = 7.06\,\text{cm}$. The H_2 flows out of the nozzle vertically and is bent downstream by the crossflow O_2 stream. The lower wall of the model combustor consists of a ramp section with an angle of 10°. Six high-bandwidth pressure transducers are mounted in plugs inserted into the centerline of the lower wall of the model combustor to allow pressure measurements.

The inflowing oxygen has an initial temperature $T_{O_2} = 1548\,\text{K}$, pressure $P_{O_2} = 0.4\,\text{bar}$ and crossflow density $U_{O_2} = 180$ cm/ms. Together with a kinematic viscosity of $\nu = 5.36 \times 10^{-3}\,\text{cm}^2/\text{ms}$, the Reynolds number for the crossflow can be computed as $Re_{O_2} = LU/\nu = 2.37 \times 10^5$, and a Kolmogorov scale $\eta_{K,O_2} = LRe^{-3/4} = 7.3$ microns.

The hydrogen is injected into the combustion chamber with a pressure $P_{H_2} = 12.5\,\text{bar}$, temperature $T_{H_2} = 300\,\text{K}$ and jet exit velocity $U_{H_2} = 113.25\,\text{cm/ms}$. Mixing occurs at the edges of the plume, leading to combustion of $2H_2 + O_2 \rightarrow H_2O$ through the detailed chemistry mechanism with eight reacting species and a total of 42 reactions. With the kinematic viscosity $\nu = 1.6 \times 10^{-4}\,\text{cm}^2/\text{ms}$, the Reynolds number $Re_{H_2} = 1.4 \times 10^5$ and corresponding Kolmogorov scale $\eta_{K,H_2} = 0.27\,\text{micron}$ are calculated.

The jet-to-crossflow momentum ratio defined as

$$J = \frac{\rho_{fuel} U_{fuel}^2}{\rho_{oxidizer} U_{oxidizer}^2} \tag{6.1}$$

characterizes the general structure of a jet in cross-flow configuration, and is

a parameter that directly affect the extent of penetration. Experiments such as [8] has been conducted to investigate the detailed flow structures with varying values of J. To be compatible with the setup given there, $J = 5$ is used in our simulations.

We use a grid spacing of $0.1\,\text{cm} \times 0.05\,\text{cm} \times 0.05\,\text{cm}$ in this simulation. It is designed to be more refined on y and z directions to reflect the fact that the mean velocity in x direction dominates the direction of the flow, therefore the characteristic length scale is much larger in the x than in the y or z directions. To increase the level of inflowing turbulence and the combustion that follows, a randomized turbulence is imposed on the injected crossflow, with a 2.3% intensity.

To model the flow turbulent motions and complicated shock structures, we use a fifth-order WENO scheme based on the finite volume discretization with an explicit third-order TVD Runge-Kutta scheme (Section 4.2), together with the dynamic LES approach (Section 3.3). The combustion is characterized by the finite rate chemistry model (Section 5.4.2).

6.2 Results and Discussions

Within the chamber, the turbulent flame is neither perfectly premixed nor perfectly non-premixed, displaying the complexities of pure mixing, partially and perfectly mixed combustion. Based on the analysis in Section 5.5.3, a thickening parameter of $TF = 8$ is chosen for the current grid size. It has already been shown there that with the finite rate chemistry model,

the current grid resolution applied to three-dimensional Scramjet combustion ($\Delta x = 0.05\,\mathrm{cm}$) would still under-resolve some major flame structures, including the amount of heat release, the start of ignition, and major species production, like OH. Here, we compare the simulation results to the ones conducted with the same parameter configurations at the Center for Turbulence Research at Stanford University. The Stanford simulation is based on a flamelet description of the flame structure, and uses an energy-conserving unstructured grid. Therefore, under comparison here are two approaches to modeling turbulent combustion, namely, the finite rate chemistry approach and the flamelet model. Figure 6.2 and Figure 6.3 compares the OH mass fraction produced using the two models. Both the $x - y$ and $x - z$ cross-sectional profiles show that combustion starts and develops in the chamber, though not as well developed as the result of the Stanford simulation.

The major discrepancy lies in the limited burning area, especially the first half of the injected hydrogen stream. This phenomena is largely due to the delay in ignition, which reduced the length of the flame zone by about 50%, but is further reduced by a nonlinear coupling of the chemistry to the hydrodynamics, and the resulting elevated stream wise flow velocity, increased by about a factor of two, further reducing the burning time by another factor of two or a total reduction to 25%. The one-dimensional analysis predicts that a thickening factor $TF = 8$ would delay the burning time by about half of the total flow time. This is consistent with both cross-sectional profiles of the OH production. Figure 6.4 and Figure 6.5

further illustrate the contour of temperature on the same two cross-sectional planes, and further show the sign of insufficient burning in the first half of the hydrogen downstream flow.

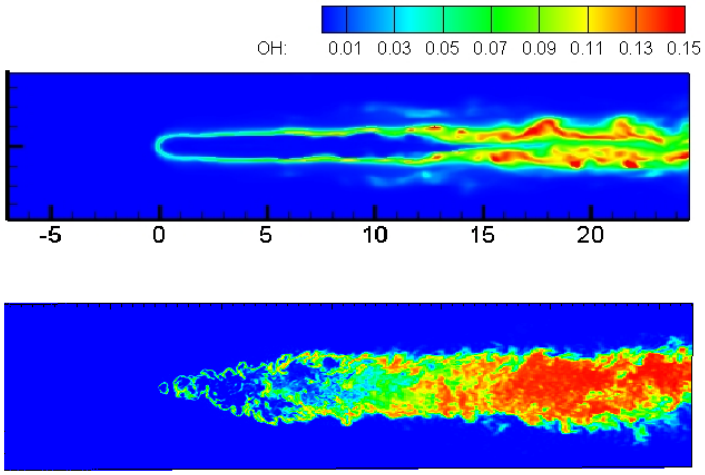

Figure 6.2: The OH mass fraction profiles in an $x - y$ plane, the slice is taken at the middle of the height of the combustor. Comparison is between the finite rate model (upper) and the flamelet model (lower).

Figure 6.6 shows the comparison of the lower wall pressure among experimental data (measurements taken at ten locations on the wall by the pressure transducers), the finite rate chemistry model and the flamelet model by Stanford, evaluated on two grid levels. As stated above, the delayed ignition time leads to about 75% loss of residence time in the combustion chamber for the flame portion of the flow. In addition, due to the nonlinear coupling between the chemistry and the hydrodynamics, the temperature and the velocity profiles are not predicted correctly. As mentioned above, the velocities are over predicted. The stream wise velocity in particular, is about two times

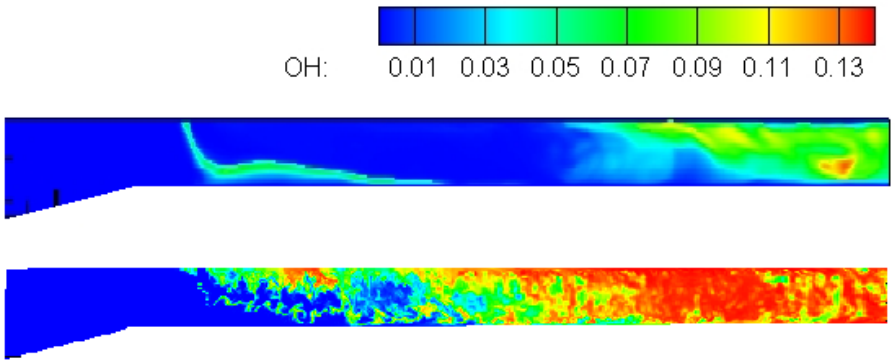

Figure 6.3: The OH mass fraction profile in an $x-z$ plane, the slice is taken at the middle of the depth of the combustor. Comparison is between the finite rate model (upper) and the flamelet model (lower).

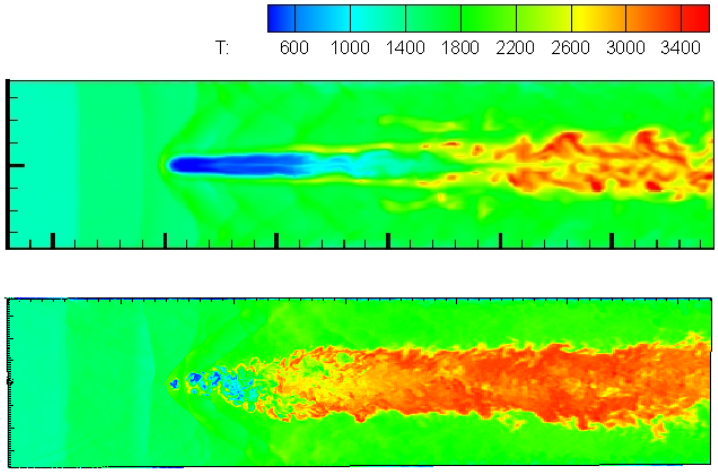

Figure 6.4: The temperature profile in an $x-y$ plane, the slice is taken at the middle of the height of the combustor. Comparison is between the finite rate model (upper) and the flamelet model (lower).

higher than predicted by Stanford's simulation results. On the other hand, the boundary layer drag on the walls is about double the amount observed in the Stanford's calculation. The combinational effect therefore leads to the

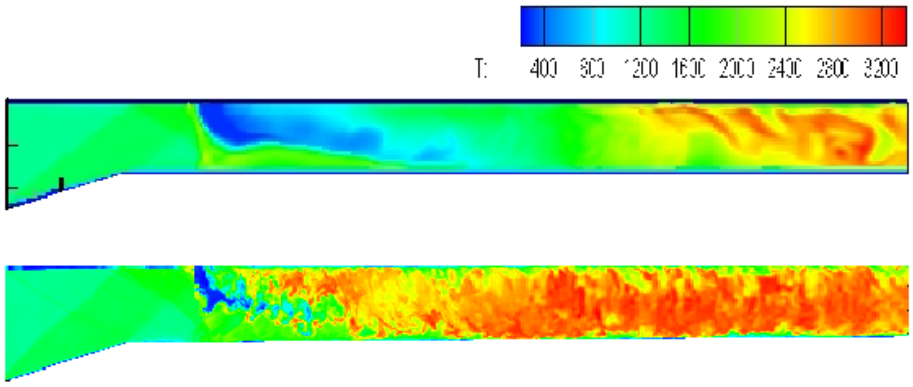

Figure 6.5: The temperature profile in an $x - z$ plane, the slice is taken at the middle of the depth of the combustor. Comparison is between the finite rate model (upper) and the flamelet model (lower).

agreement of wall pressures with experimental data, but due to canceling errors.

Table 5.6 indicates the minimum mesh requirements after applying a combination of the thickened flame model and a possible reduced chemistry level. The delay in ignition could be reduced to 7% and 0% for a full and reduced chemical mechanism, respectively, within the considered range of mesh sizes. Based on the one dimensional analysis, at least the second case would lead to a correct calculation. The predicted minimum mesh size without a delay in ignition is therefore a $\Delta x = 0.02\,\text{cm}$ with reduced chemistry, and a $\Delta x = 0.01\,\text{cm}$ with full chemistry and thickening factor $TF = 1$ (no thickening).

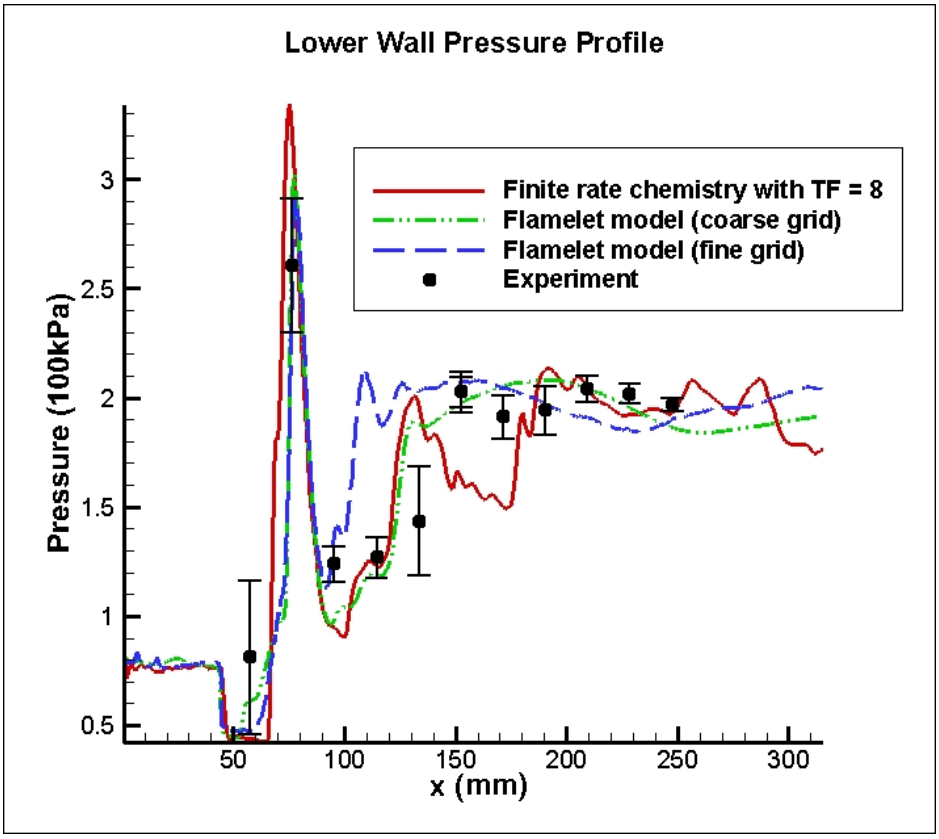

Figure 6.6: The lower wall pressure, compared among experimental data, finite rate chemistry model and the flamelet model by Stanford evaluated on two grid levels.

7 Conclusions

In this work, we study the turbulent mixing and combustion of the supersonic flow using Large Eddy Simulation. Our main focus is to determine mesh requirements needed to employ finite rate chemistry model. The combustion process modeled by the finite rate chemistry approach is based on the notion that chemical processes have length scales orders of magnitude larger than

the smallest turbulence scales, and therefore could be resolved on a coarser grid. The one-dimensional studies presented in Section 5.5.3 confirms that chemistry could be resolved with a grid on the order of 10^{-2} cm. Moreover, to compensate for the deficiencies in resolving combustion, and to reduce computational cost (a challenge to be faced when using more refined grids), it could be useful to apply the thickened flame model and a reduced chemical mechanism. Section 6 presents a three-dimensional Scramjet simulation with the grid resolution $\Delta x = 0.05$ cm. It can be concluded from the simulation results that $\Delta x = 0.05$ cm is still not refined sufficiently to obtain a fully developed flame. To reach that objective, our one-dimensional flame analysis predicts that a mesh refinement down to $\Delta x = 0.02$ cm with the reduced chemical mechanism and no thickening could succeed.

References

[1] A. R. T.F. Fric, "Vortical structure in the wake of a transverse jet," *J. Fluid Mech.*, vol. 279, pp. 1–47, 1994.

[2] A. P. R.M. Kelso, T.T. Lim, "An experimental study of round jets in cross-flow," *J. Fluid Mech.*, vol. 306, pp. 111–144, 1996.

[3] M. M. S.H. Smith, "Mixing, structure and scaling of the jet in crossflow," *J. Fluid Mech.*, vol. 357, pp. 83–122, 1998.

[4] L. K. J. Ziefle, "Large-eddy simulation of a round jet in crossflow," *AIAA Journal*, vol. 47, pp. 1158–1172, 2009.

[5] K. M. S. Muppidi, "Study of trajectories of jets in crossflow using direct numerical simulations," *J. Fluid Mech.*, vol. 530, pp. 81–100, 2005.

[6] A. R. Karagozian, "Transverse jets and their control," *Progress in Energy and Combustion Science*, vol. 36, pp. 531–553, 2010.

[7] S. R. Yuan LL, "Trajectory and entrainment of a round jet incrossflow," *Physics of Fluids*, vol. 10, pp. 2323–2335, 1998.

[8] R. K. H. Mirko Gamba, M. Godfrey Mungal, "OH PLIF imaging of the reaction zone in combusting transverse jets in supersonic crossflow," July 2012.

[9] H. N. E. Smart, M. K. and A. Paull, "Flight data analysis of the hyshot 2 scramjet flight experiment," *AIAA Journal*, vol. 44, no. 10, pp. 2366–2375, 2006.

[10] A. P. A. D. Gardner, K. Hannemann and J. Steelant, "Ground testing of the hyshot supersonic combustion flight experiment in heg," *Shock Waves, Proceedings of the 24th International Symposium on Shock Waves Beijing, China*, pp. 329–334, July 2005.

[11] R. K. H. Mirko Gamba, M. Godfrey Mungal, "Ignition and near-wall burning in transverse hydrogen jets in supersonic crossflow," *49th AIAA Aerospace Sciences Meeting including the New Horizons Forum and Aerospace Exposition*, January 2011.

[12] M. G. G. M. Victor Miller, Mirko Gamba and R. K. Hanson, "Development of a model scramjet combustor," in *49th AIAA Aerospace Sciences Meeting including the New Horizons Forum and Aerospace Exposition*, January 2011.

[13] F. H. R. Pecnik, V. E. Terrapon and G. Iaccarino, "Full system scramjet simulation," *Annual Research Briefs*, 2009.

[14] R. V. J. Larsson and I. Bermejo-Moreno, "Large eddy simulation of the Hyshot II scramjet," *Annual Research Briefs*, 2011.

[15] B. E. M. J. W. N. A. Hadjadj, J. Larsson and S. K. Lele, "Large-eddy simulation of shock/boundary-layer interaction," *Proceedings of the Summer Program*, pp. 141–152, 2010.

[16] G. S. S. M. P. W. K. P. K. T. J. P. A. X. Sengissen, A. V. Giauque, "Large eddy simulation of piloting effects large eddy simulation of piloting effects on turbulent swirling flames," *Proceedings of the Combustion Institute*, vol. 31, pp. 1729–1736, 2007.

[17] H. S. M. Debasis Chakraborty, P. J. Paul, "Evaluation of combustion models for high speed H2/air confined mixing layer using dns data," *Combustion and Flame*, April 2000.

[18] A. T. H. R. A. Baurle and H. A. Hassan, "Assumed and evolution probability density functions in supersonic turbulent combustion calculations," *Journal of Propulsion and Power*, vol. 11, no. 6, pp. 1132–1138, 1995.

[19] S. S. G. R. A. Baurle, "Assumed PDF turbulence-chemistry closure with temperature-composition correlations," *Combustion and Flame*, vol. 134, pp. 131–148, 2003.

[20] R. P. V. E. Terrapon, F. Ham and H. Pitsch, "A flamelet-based model for supersonic combustion," *Annual Research Briefs*, 2009.

[21] J. E. M. Alexandre Chorin, *A Mathematical Introduction to Fluid Mechanics*. Springer-Verlag, third ed., 2000.

[22] A. N. Kolmogorov, "The local structure of turbulence in incompressible viscous fluid for very large reynolds numbers," *Proceedings of the Royal Society A*, vol. 434, pp. 9–13, 1991.

[23] U. Frisch, *Turbulence: The legacy of A. N. Kolmogorov*. 1995.

[24] T. B. G. K. H. J. S. T. J. C. P. A. D. B. A. P. M. L. F.-S. L. Y. N. J. F. W. R. C. C. D. R. D. L. B. I. R. J. X. W. A. M. S. S. B. J.-P. B. W. P. J. K. H. S. K. G. N. C. B. J. G. A. L. B. E. Launder, N. D. Sandham, *Closure Strategies for Turbulent and Transitional Flows*. 2004.

[25] G. M., "Turbulence: the filtering approach," *J. Fluid Mech.*, vol. 238, pp. 325–336, 1992.

[26] W. C. P. Moin, K. Squires and S. Lee, "A dynamic subgrid-scale model for compressible turbulence and scalar transport," *Phys. Fluids A*, vol. 3, no. 2746-2757, 1991.

[27] S. J., "General circulation experiments with the primitive equations. I. The basic experiment.," *Mon. Weather Rev.*, vol. 91, no. 99-164, 1963.

[28] G.-S. Jiang and C.-W. Shu, "Efficient implementation of weighted ENO schemes," tech. rep., Institute for Computer Applications in Science and Engineering, 1995.

[29] D. V. Thierry Poinsot, *Theoretical and Numerical Combustion*. R.T. Edwards, Inc., second edition ed., 2005.

[30] D. R. Lide, *CRC Handbook of Chemistry and Physics*, 95th ed., 2014.

[31] B. R. B. Hirschfelder J, Curtiss C. F, *Molecular Theory of Gases and Liquids*. John Wiley & Sons, Inc., 1954.

[32] K. O. F. R. Courant, *Supersonic Flow and Shock Waves*. Applied Mathematical sciences, Springer, 1999.

[33] M. A. R. Bonnie J. McBride, Sanford Gordon, "Coefficients for calculating thermodynamic and transport properties of individual species," tech. rep., National Aeronautics and Space Administration, 1993.

[34] F. J. S. P. H. Max Klein, H. J. M. Hanley, "Tables of collision integrals and second virial coefficients for the (m, 6, 8) intermolecular potential function," tech. rep., National Bureau of Standards, June 1974.

[35] F. C. for Compuational Science, *FLASH User's Guide*. University of Chicago, Februry 2012.

[36] R. S. Brokaw, "Viscosity of gas mixtures," tech. rep., Lewis Research Center, April 1968.

[37] F. A. W. Priyank Saxena, "Testing a small detailed chemical-kinetic mechanism for the combustion of hydrogen and carbon monoxide," *Combustion and Flame*, vol. 145, pp. 316–323, April 2006.

[38] J. Troe, "Towards a quantitative understanding of elementary combustion reactions," *Proceedings of the Combustion Institute*, vol. 22, pp. 843–862, 1988.

[39] F. A. W. G. BALAKRISHNAN, M. D. SMOOKE, "A numerical investigation of extinction and ignition limits in laminar nonpremixed counterflowing hydrogen-air streams for both elementary and reduced chemistry," *Combustion and Flame*, vol. 102, pp. 329–340, 1995.

[40] Center for Turbulence Research, *Dynamically thickened flame LES model for premixed and non-premixed turbulent combustion*, 2000.

[41] M. D. S. J. A. M. R. J. Kee, J. F. Grcar and E. Meeks, *PREMIX: A Fortran Program for Modeling Steady Laminar One-Dimensional Premixed Flames*. Reaction Design, 11436 Sorrento Valley Road, April 1998.

[42] M. D. Smooke, "The computation of laminar flames," *Proceedings of the Combustion Institute*, vol. 34, pp. 65–98, 2013.

[43] D. V. O. Colin, F. Ducros and T. Poinsot, "A thickened flame model for large eddy simulations of turbulent premixed combustion," *Physics of Fluids*, vol. 12, pp. 1843–1863, July 2000.

[44] D. V. C. Angelberger and F. Egolfopoulos, "LES of chemical and acoustic forcing of a premixed dump combustor," *Flow, Turbulence and Combustion*, vol. 65, pp. 205–222, 2000.

[45] A. M. K. Fabian Proch, "Numerical analysis of the cambridge stratified flame series using artificial thickened flame LES with tabulated premixed flame chemistry," *Combustion and Flame*, vol. 161, pp. 2627–2646, 2014.

[46] F. A. Williams, "Detailed and reduced chemistry for hydrogen autoignition," *Journal of Loss Prevention in the Process Industries*, vol. 21, pp. 131–135, 2008.

[47] A. L. F. W. D. Fernandez-Galisteo, A.L. Sanchez, "One-step reduced kinetics for lean hydrogen-air deflagration," *Combustion and Flame*, vol. 156, pp. 985–996, 2009.

[48] C. J. B. C. Pierre Boivin, Antoine Dauptain, "Simulation of a supersonic hydrogen–air autoignition-stabilized flame using reduced chemistry," *Combustion and Flame*, vol. 159, pp. 1779–1790, 2012.

[49] *J. Larsson. Private communication. 2012 - 2013.*